# The Journal of Undergraduate Research in Physics




*Volume 16, Number 2*
*Spring, 1998*

Produced by the Physics Department of Guilford College
for
The American Institute of Physics and the Society of Physics Students

# *THE JOURNAL OF UNDERGRADUATE RESEARCH IN PHYSICS*

This journal is devoted to research work done by undergraduate students in physics and its related fields. It is to be a vehicle for the exchange of ideas and information by undergraduate students. Information for students wishing to submit manuscripts for possible inclusion in the Journal follows.

**ELIGIBILITY**
The author(s) must have performed all work reported in the paper as an undergraduate student(s). The subject matter of the paper is open to any area of pure or applied physics or physics related field.

**SPONSORSHIP**
Each paper must be sponsored by a full-time faculty member of the department in which the research was done. A letter from the sponsor, certifying that the work was done by the author as an undergraduate and that the sponsor is willing to be acknowledged at the end of the paper, must accompany the manuscript if it is to be considered for publication.

**SUBMISSION**
Two copies of the manuscript, the letter from the sponsor and a telephone number or E-Mail address where the author can be reached should be sent to:
Dr. Rexford E. Adelberger, Editor
THE JOURNAL OF UNDERGRADUATE RESEARCH IN PHYSICS
Physics Department
Guilford College
Greensboro, NC 27410

**FORM**
The manuscript should be typed, double spaced, on 8 1/2 x 11 inch sheets. Margins of about 1.5 inches should be left on the top, sides, and bottom of each page. Papers should be limited to fifteen pages of text in addition to an abstract (not to exceed 250 words) and appropriate drawings, pictures, and tables. Manuscripts may be submitted on a disk that can be read by a MacIntosh™. The files must be compatible with MacWrite™, MicroSoft Word™ , PageMaker™ or WordPerfect™.

**ILLUSTRATIONS**
Line drawings should be made with black ink on plain white paper. The line thickness should be sufficient to be reduced to column format. Each figure or table must be on a separate sheet. Photographs must have a high gloss finish. If the submission is on a disk, the illustrations should be in PICT, TIFF or EPS format.

**CAPTIONS**
A descriptive caption should be provided for each illustration or table, but it should not be part of the figure. The captions should be listed together at the end of the manuscript

**EQUATIONS**
Equations should appear on separate lines, and may be written in black ink. All equations should be numbered. We use EXPRESSIONIST™ to format equations in the Journal.

**FOOTNOTES**
Footnotes should be typed, double spaced and grouped together in sequence at the end of the manuscript.

**PREPARING A MANUSCRIPT**
A more detailed set of instructions for authors wishing to prepare manuscripts for publication in the Journal of Undergraduate Research in Physics can be found in the back of each issue.

## SUBSCRIPTION INFORMATION

The Journal is published twice each academic year, issue # 1 appearing in the fall and issue # 2 in the spring of the next calendar year. There are two issues per volume.

| TYPE OF SUBSCRIBER | PRICE PER VOLUME |
|---|---|
| Individual | $US 5.00 |
| Institution | $US 10.00 |

Foreign subscribers add $US 2.00 for surface postage, $US 10.00 for air freight.

Back issues may be purchased by sending $US 15.00 per volume to the editorial office.

To receive a subscription, send your name, address, and check made out to **The Journal of Undergraduate Research in Physics (JURP)** to the editorial office:

JURP
Physics Department
Guilford College
Greensboro, NC 27410

**The Journal of Undergraduate Research in Physics** is sent to each member of the Society of Physics Students as part of their annual dues.

# MAGNETIZATION OF STRAINED COBALT FILMS AND THE MAGNETO-OPTIC KERR EFFECT

Elizabeth Mayo
Department of Physics
West Virginia University
Morgantown, WV 26506-6315
received June 10, 1997

**ABSTRACT**

Using the magneto-optic Kerr effect, it was possible to detect changes in the shape of magnetic hysteresis loops due to stress applied to ferromagnetic polycrystalline cobalt thin films. When stress was applied to cobalt thin films , the remanent magnetization increased perpendicular to the direction of the stress. This result is consistent with other studies of the effect of stress applied to bulk polycrystalline cobalt.

## INTRODUCTION

The surface magneto-optic Kerr effect (SMOKE) was first used in 1985 to measure the magnetization of Fe films deposited on gold. [1] It since has become an important tool in this area of study. It has been used to search for magnetic ordering, to identify dominant magnetic anisotropies and to characterize the critical magnetization exponent at two dimensional phase transitions. [1]

The surface magneto-optic Kerr effect occurs when linearly polarized light is reflected from the surface of a magnetized medium. The light decomposes into left and right circularly polarized modes. The two modes have different indices of refraction, travel with different velocities and attenuate differently. When the two modes reflect from the material, they recombine to yield a rotated polarization and ellipticity. [2] The magneto-optic interaction causes the electric field vector of the light to rotate. The induced response has two components: an inphase part that causes the rotation and an out-of-phase part that causes the ellipticity.

When the magnetization of the material is reversed, the magneto-optic rotation and ellipticity reverse sign. This can be achieved in a ferromagnetic sample by reversing the external magnetizing field. The change in polarization is measured by measuring the intensity of the reflected beam after it passes through a linear polarizing analyzer. The intensity of the transmitted signal is:

$$I = I_o \cos^2(\phi) \ , \qquad (1)$$

where $\phi$ is the angle between the polarization of the beam and the axis of the analyzer and $I_o$ is the incident intensity of the reflected beam. Differentiating Equation 1 with respect to the angle $\phi$ gives:

$$\frac{dI}{d\phi} = -\sin(2\phi) \ . \qquad (2)$$

Hence, the Kerr signal, $dI$, is proportional to the change in the rotation of the polarization of the light, $d\phi$. The signal produced by the SMOKE during the reversal of the magnetic field is proportional to the sample's magnetization. [2]

*Elizabeth is a senior physics major at West Virginia University. This research was begun during the spring semester of her junior year as an advanced physics laboratory project and has continued throughout her senior year. The results were presented at the March meeting of the American Physical Society in a poster session. Currently she is looking forward to attending graduate school in astronomy.*

## THE EXPERIMENT

This experiment was designed to observe the effects of stress on a ferromagnetic sample using SMOKE. A magnetization curve for a sample was generated using the SMOKE technique. The direction of the stress was varied and the magnetization curves compared with those of the unstressed samples. This allowed us to observe how the stress affected the magnetization of the sample.

*Sample preparation and characterization*

All films in this study were prepared by magnetron sputtering on mica substrates at an argon sputtering pressure of 3.0 mTorr in a chamber with a base pressure of 1 μTorr. The sample holder, outfitted with a heater, was centered about four sputtering guns. Mica was chosen as

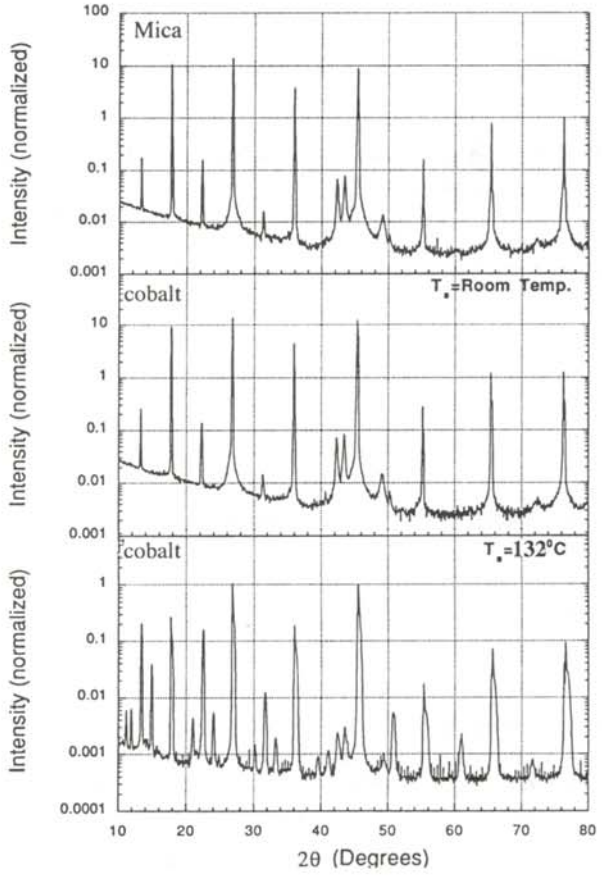


*Figure 1*
*X-ray intensity vs 2θ for a pure mica substrate and the Co thin films. The peaks represent Bragg diffraction from atomic planes. $T_S$ is the growth temperature for the samples: A ($T_S$=room temperature), B ($T_S$ = 132 C).*

the substrate due to its flexibility. The ferromagnetic metal chosen for this study was cobalt. Two samples were produced, one at room temperature and one at 132 C.

The films were characterized by large angle Cu $K_\alpha$ ($\lambda$ = 0.15418 nm) X-ray diffraction and small angle X-ray reflectivity using a rotating anode diffractometer equipped with a four-circle goniometer. Large angle X-ray diffraction is sensitive to interplanar lattice spacings consistent with Bragg's law:

$$2\,d\sin(\theta) = n\,\lambda\ , \qquad (3)$$

where $d$ is the lattice spacing between the planes, $\theta$ is the angle of incidence with respect to the atomic planes and $\lambda$ is the X-ray wavelength. Small angle reflectivity scans were performed to characterize the film's surface rough and thickness. Small angle X-ray reflectivity is sensitive to these properties due to the X-ray interference between the top and bottom surfaces of the film. The film thickness was calculated from the minima of the reflectivity scans using the relationship:

$$\sin^2(\theta) = \left(\frac{n\,\lambda}{2\,D}\right)^2 + 2\,\delta\ , \qquad (4)$$

where $D$ is the film thickness, $\delta$ is the real part of the index of refraction. [3]

Figure 1 shows the large angle X-ray diffraction scans of the mica substrate (Figure 1a), cobalt sample-A (Figure 1b) and cobalt sample-B (Figure 1c). For each sample the Bragg peaks were compared to those of the mica substrate. Cobalt has a face centered cubic (fcc) crystal structure. Cobalt sample-A, grown at room temperature, did not exhibit any Bragg peaks expected from a single fcc crystal. Its scan matched that of the mica substrate quite well. This implies that sample-A did not exhibit growth along a particular crystallographic direction and, therefore, is likely to be polycrystalline (made up of many small randomly oriented crystals).

Cobalt sample-B, grown at 132 C, showed a Bragg peak corresponding to scattering by the {002} planes in Co. (2θ = 51.8 °). There were also other peaks which did not correspond to cobalt or mica. These could have been due to the cobalt film forming an alloy at the surface of the substrate or the heating process changing the crystal structure of the mica substrate. Sample-B, therefore, is a fcc cobalt film oriented along the [001] direction.

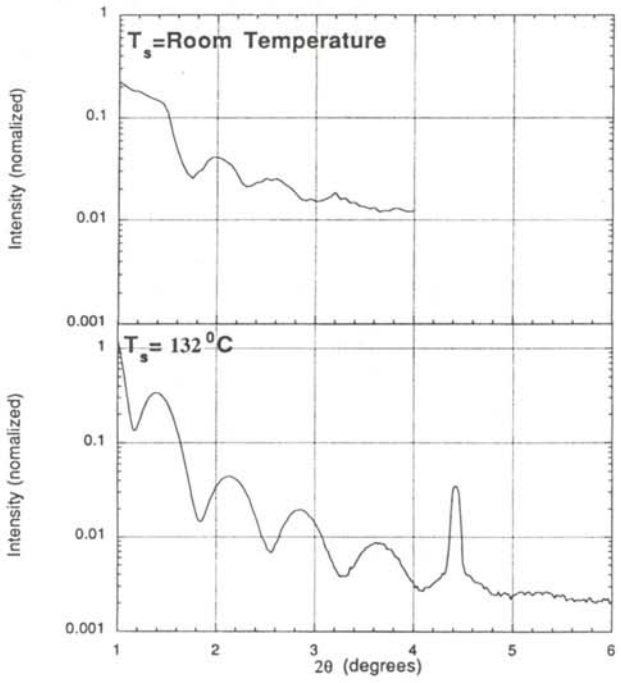


*Figure 2*
*X-ray intensity vs 2θ for Co samples. Peaks represent interference between X-rays from the top and bottom of the films. $T_S$ is the growth temperature for the samples: A ($T_S$=room temperature), B($T_S$ = 132 C). The sharp peak near 2θ = 4.4° is due to a Bragg reflection from an atomic plane in mica.*

The small angle X-ray diffraction results are shown in Figure 2. Sample-A shows very few peaks. In comparison, sample-B has many high intensity peaks. From this, one concludes that sample B has a smoother film surface than sample A. The film thickness were calculated using Equation 2. Sample-A, grown at room temperature was approximately 10.4 nm thick, while sample-B, grown at 132 C, was 11.1 nm thick. The estimate for the thickness of Sample-B was more accurate than that for Sample-A due to the greater number of minima present in the scan.

**Kerr Rotation Measurement**

A semiconductor laser ($\lambda = 670$ nm) was used as the light source. The incident light was linearly polarized by a polarizer in the plane of incidence. The sample was placed between the poles of an electromagnet, producing the external magnetic field, $H$. The light reflected from the sample passed through an analyzing polarizer set 2° from extinction. The Kerr signal was detected by a photomultiplier tube (PMT). The current output of the PMT was amplified and converted into a voltage. To reduce the noise to signal ratio, it was necessary to focus the beam to a point onto both the sample and the PMT. We used a quarter wave plate to remove some of the ellipticity induced by the birefringence of the mica substrate.

The bipolar power supply of the magnet was computer controlled by a program which regulated the current of the magnet. The program also recorded the output of the PMT and the output of a Gauss meter placed between the poles of the magnet. Figure 3 is a schematic diagram of the experimental setup.

To make sure that the Kerr signal loop was observed only in magnetic material, we measured the magnetization loop of a nonmagnetic Re thin film and compared it with the magnetization loop of a known ferromagnetic Fe sample. Both films were grown on a sapphire substrate. Figure 4 is a plot of the ratio of the measured intensity with magnetic field $H$, $I(H)$, to the measured intensity at saturation, $I_S$ for the Re sample. The magnetization loop showed no

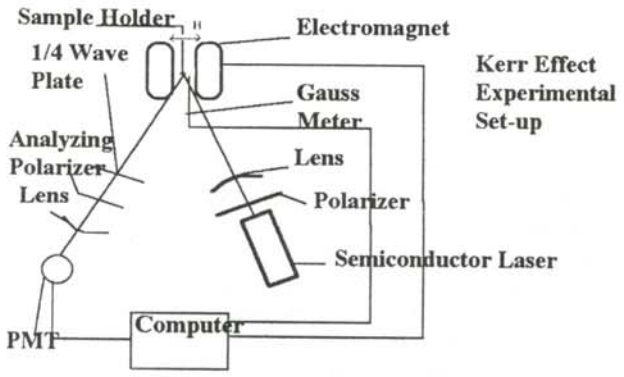


*Figure 3*
*Schematic diagram of the Kerr rotation experimental setup.*

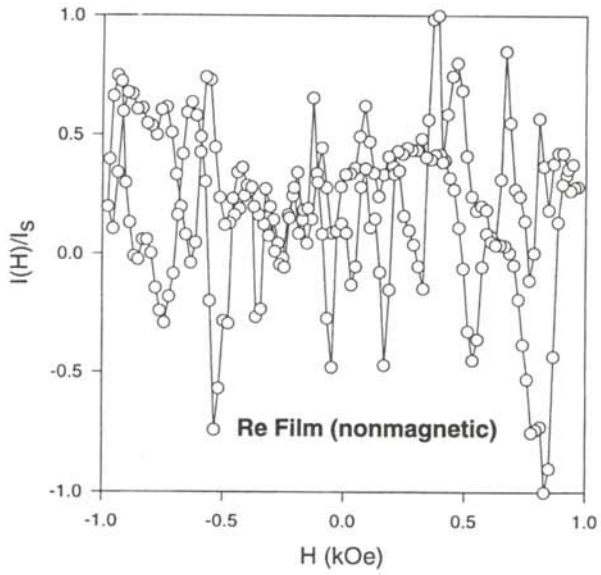


*Figure 4*
*Normalized (to saturation) light intensity vs. magnetic field, H, for a nonmagnetic Re thin film.*

magnetization curve, while the results from the Fe sample, shown in Figure 5, showed a definite magnetization curve.

*Effects of Stress on the magnetization loops*

Each of the cobalt samples first placed on a flat sample holder and were measured in an unstressed state. A stress was then induced on the samples by mounting them on the curved surface of a cylindrical sample holder as shown in Figure 6. The stress, $\sigma$, on the samples is given by [4]:

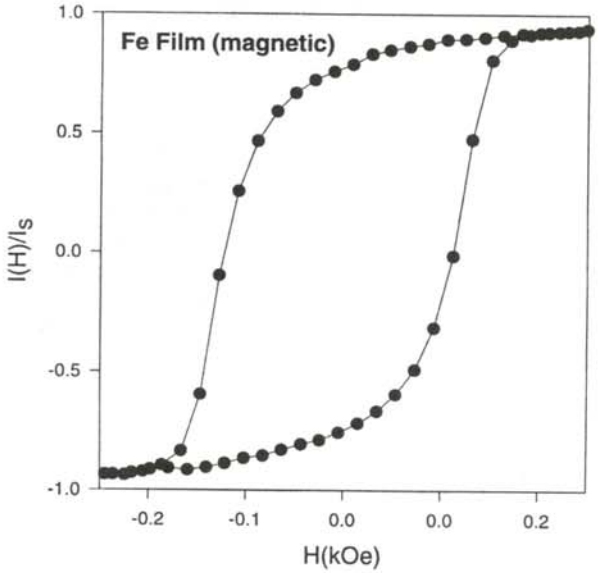


*Figure 5*
*Normalized (to saturation) light intensity vs Magnetic field, H, for a ferromagnetic Fe thin film.*

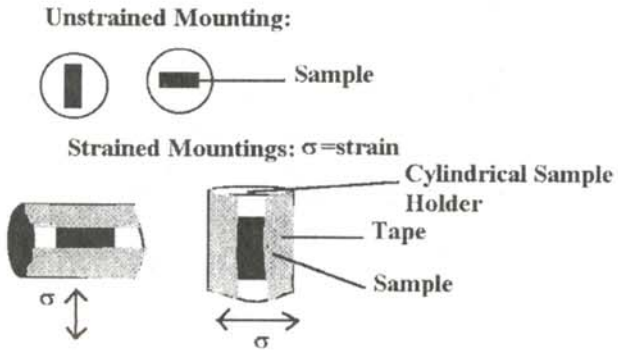


*Figure 6*
*Diagram showing the sample stress direction with respect to the magnetic field, H. The strained mounting diagram shows samples stressed along the long (a) and short (b) directions. The cylinder could be rotated about the surface of the film to measure the Kerr signal with H perpendicular or parallel to the stress σ.*

$$\sigma = \frac{\Delta F}{\Delta A} = Y\left(\frac{y}{R}\right), \qquad (5)$$

where $Y$ is Young's modulus of Co (200 x $10^9$ Pa) [5], $R$ is the radius of the sample holder (1.905 cm) and $y$ is the thickness of the substrate (neglecting the film thickness (0.025mm). The stress applied to the sample was 1.31 x $10^6$ Pa (13.4 kg/mm$^2$).

The films were rectangular in shape, with short and long axes perpendicular to each other. For each sample, six magnetization loops were measured:

a) (unstressed) flat with $H$ parallel and perpendicular to the short sample axis.
b) stressed along the short sample axis, with $H$ parallel and perpendicular to the short sample axis.
c) Stressed along the long sample axis, with $H$ parallel and perpendicular to the short sample axis.

## RESULTS

Figures 7 and 8 show the changes in the light intensity (the Kerr signal), normalized to the saturation value, of samples A and B in the different configurations. For both samples in the unstressed state, the remanent magnetization (magnetization at H = 0) was smaller in one direction than the other. The remanent magnetization of the loops was different when $H$ was applied parallel and perpendicular to the short axis of the sample.

When the samples were stressed, the magnetization curves changed. Both samples exhibited a change in the remanent magnetization of the loop with the applied strain. This is shown in Figures 7 and 8 by the increased remanent magnetization of the magnetic hysteresis curves when the stress is applied perpendicular to $H$ and the decrease in remanent magnetizations of the curves when the stress is applied parallel to $H$.

This effect can be quantified by calculating the normalized remanent magnetization. The normalized remanent magnetization, $(M_R/M_S)$, is the ratio of the magnetization

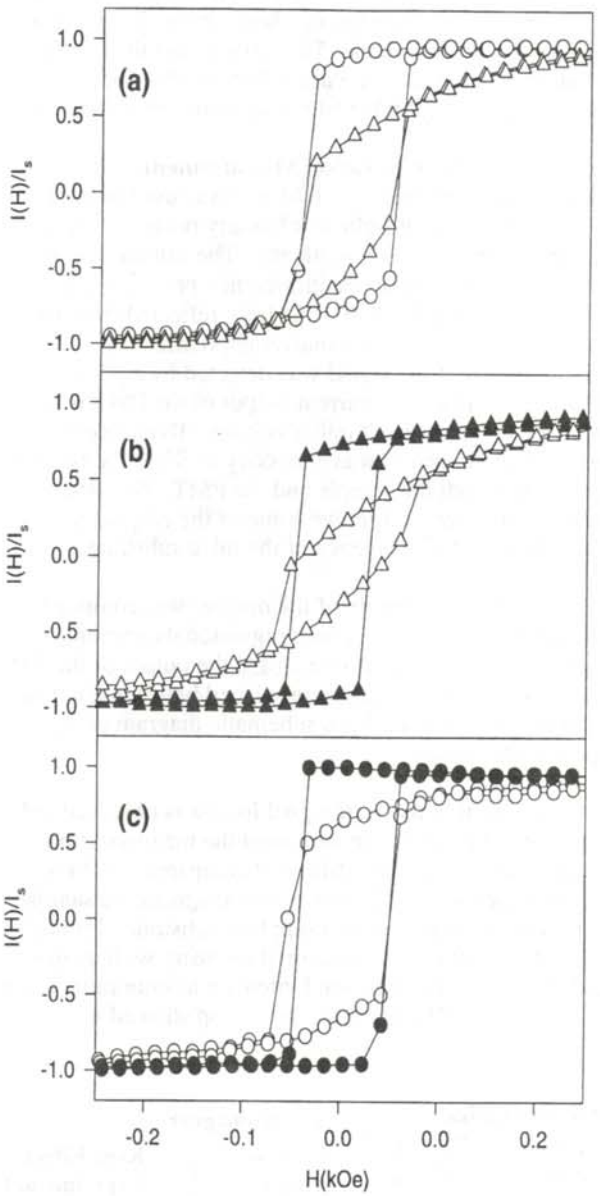


*Figure 7*
*Normalized (to saturation) light intensity vs magnetic field, H, for Co sample A. The circles represent data measured with H perpendicular to the short axis of the rectangular sample and the triangles represent data measured with H parallel to the short axis of the rectangular sample. Graph (a) is data measured in the unstressed configuration. In graphs (b) and (c), the shaded figures represent data obtained with the stress applied perpendicular to H and the unshaded figures represent data obtained with the stress applied parallel to the magnetic field.*

at $H$=0, $M_R$ ,to the magnetization at saturation, $M_S$. We assume that:

$$\frac{M_R}{M_s} = \frac{I(H=0)}{I_S} \quad . \tag{6}$$

Table 1 shows the values of the normalized remanent magnetization for both samples A and B. The changes in the $M_R/M_S$ values reflect the changes in the shapes of the magnetization loops for each sample.

These results indicate that stress induces an increase in the remanent magnetization in cobalt films perpendicular to the direction of the strain. The results for both samples studied are similar to each other, despite the differences in their surface morphology and crystallinity. Our results agree with those found by others who have studied the effect of stress applied to bulk polycrystalline Co. [5]

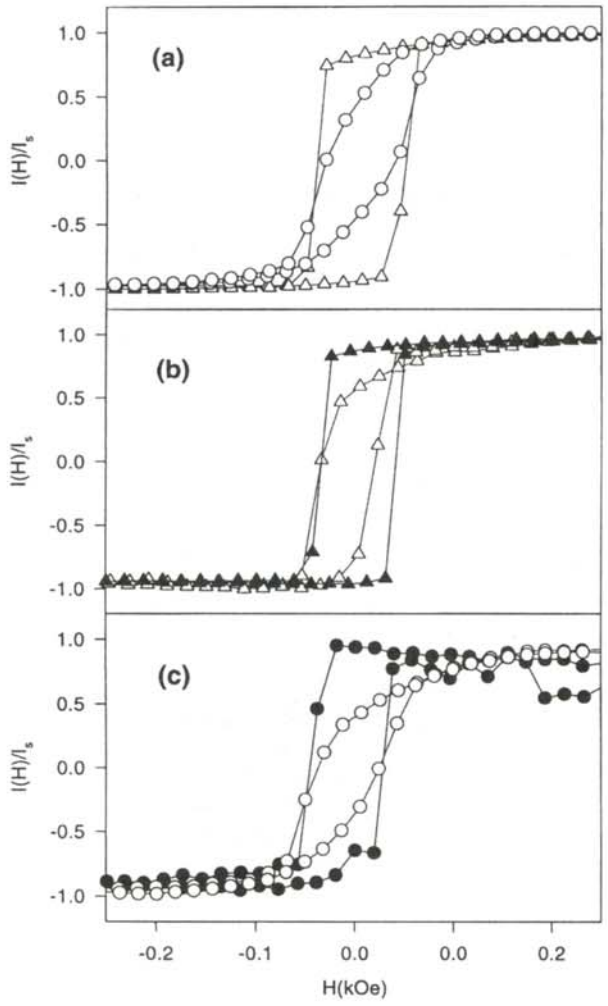


*Figure 8*
*Normalized (to saturation) light intensity vs magnetic field, H, for Co sample B. The circles represent data measured with H perpendicular to the short axis of the rectangular sample and the triangles represent data measured with H parallel to the short axis of the rectangular sample. Graph (a) is data measured in the unstressed configuration. In graphs (b) and (c), the shaded figures represent data obtained with the stress applied perpendicular to H and the unshaded figures represent data obtained with the stress applied parallel to the magnetic field.*

| Stress Direction | $M_R/M_S$ | | | Sample |
|---|---|---|---|---|
| | Unstressed | $\sigma \perp H$ | $\sigma \parallel H$ | |
| H ∥ to short axis | 0.33 | 0.72 | 0.20 | A |
| H⊥ to short axis | 0.89 | 1.00 | 0.65 | A |
| H ∥ to short axis | 0.81 | 0.87 | 0.53 | B |
| H⊥ to short axis | 0.40 | 0.94 | 0.40 | B |

*Table 1*
*Normalized remanent magnetization ($M_R/M_S$) for each Co sample, showing the effect of the applied stress, $\sigma$, on the magnetization of the sample. The Kerr signal was measured with H either parallel or perpendicular to the short axis of the rectangular films. H was pointing along the surface of the film in both cases. The stressed sample was placed in the magnetic field with the direction of the stress parallel and perpendicular to the magnetic field.*


## ACKNOWLEDGMENTS

The author would like to thank Dr. David Lederman for his help and advice, Dr. Tom Myers for his help with the equipment setup, Dr. Nancy Giles for providing some optics equipment, Dr. Mark Koepke for providing the magnet power supply and Tim Charlton for help with growing the samples. This work was funded in part by the West Virginia Space Grant Consortium and the West Virginia University Physics Department.


## REFERENCES


1. E.R. Moog and S.D. Bader, Superlattice Microstruct. 1, (1985), p. 543; S.D. Bader, E.R. Moog and P. Grunberg, J. Magn. Magn. Mater., 53, (1986), p. L295; S.D. Bader and E.R. Moog, J. Appl. Phys, 61, (1987), p. 3729.
2. S.D. Bader, J. Magn. Magn. Mater., 100, (1991), p.442.
3. E.E. Fullerton, I.K Schuller, H. Vanderstaeten and Y. Bruynseraede, Phys. Rev., B, 45, (1991), p. 9292.
4. Feynman, Leighton and Sands, The Feynman Lectures on Physics, (Addison-Wesley Publishing Co., Reading MA), 1964, p. 38-2.
5. R. Bozorth, Ferromagnetism, (D. Van Nostrand Co., Inc., Princeton, NJ), 1951, p. 262, p. 635.


## FACULTY SPONSOR


Dr. David Lederman
Department of Physics
West Virginia University
Morgantown, WV 26506-6315
dlederma@wvu.edu

# INVESTIGATION OF CHANGES IN SURFACE MORPHOLOGY OF RUTILE TITANIUM DIOXIDE DURING REDUCTION

Brian Bradford and John Kassay
Department of Physics and Engineering
Ft. Lewis College
Durango, CO 81301
received Dec 8, 1997

**ABSTRACT**

Single crystal rutile (a tetragonal structure) titanium dioxide ($TiO_2$) samples are routinely reduced at high temperature in an oxygen poor environment to make them semiconducting for applications in photocatalysis. Such reduction is not generally thought to drastically change the surface structure of $TiO_2$. As a consequence, reduced samples are often used for studies of the properties of single crystal surfaces. We examined the surface features of rutile $TiO_2$ before and after reduction at approximately 500 C using atomic force microscopy. Significant surface roughening and possible facet formation are seen on both the (110) and (001) faces of $TiO_2$ crystals after reduction. These results suggest that reduced surfaces are no longer single crystal in nature.

## INTRODUCTION

Titanium dioxide, $TiO_2$ , is most widely used around the world as a pigment in white paint, and is even used as the whitener in nondairy creamer. In recent years, it has been investigated as a material that uses light energy to catalyze chemical reactions, a photocatalyst. It could be used as a photocatalyst to harness solar energy, trigger organic synthesis reactions and to purify water and air. [1,2]

$TiO_2$ is a structure with three titanium atoms around each oxygen atom and six oxygen atoms around each titanium atom. There are three different crystal structures that have this stoichiometry: rutile, anatase and brookite. The rutile form, which is the most stable, has a tetragonal structure. [3] $TiO_2$ in its rutile form is very non-reactive and nonconductive. When a $TiO_2$ sample is reduced by placing the crystal in an oxygen deprived environment at 500 C for approximately 4 hours, the oxygen atoms are driven out of the $TiO_2$ lattice, leaving behind defects that increase conductivity. The reduced sample is an n-type semiconductor. The band gap of reduced rutile $TiO_2$ is 3.1 eV, making it capable of breaking down many organic substances when illuminated by ultra violet light. [5] When UV light is shined on $TiO_2$, an electron is excited from the valence band across the band gap and into the conduction band. This electron is then available to induce a reduction process that breaks down organic compounds.

Reduced $TiO_2$ samples are used as "single crystal" surfaces to study structure and properties of the surfaces. It is possible to select $TiO_2$ surfaces that have different atomic orientation and, thus, different properties. Such surfaces are obtained by cutting a crystal of $TiO_2$ along one of several planes to expose the desired orientation. We chose to study crystals that had either (110) or (001) crystal faces exposed. Surfaces such as this can facet, a process where once crystal face 'kinks' or re-orders to form another orientation. Usually it takes high temperatures to induce faceting. For our surfaces, some faceting has been observed, but at much higher temperatures [6,7] than we used to reduce our samples. Thus, our samples are generally assumed to be single crystal.

*Brian is a junior chemical engineering major at Fort Lewis College. He plans to transfer to Colorado School of Mines to complete his B.Sc. and M.Sc. in the fall of 1998. This research was completed as part of a summer research internship sponsored by the Colorado Alliance for Minority Participation. Brian's spare time is devoted to studying, playing basketball and spending time with his family.*

*John is a junior physics major at Fort Lewis College. He is simultaneously finishing his B.Sc. and running a successful cabinet shop. He did this research as part of a summer research internship sponsored by the Colorado Space Grant Consortium. In his spare time, John likes to rock climb and hike in the Colorado mountains.*

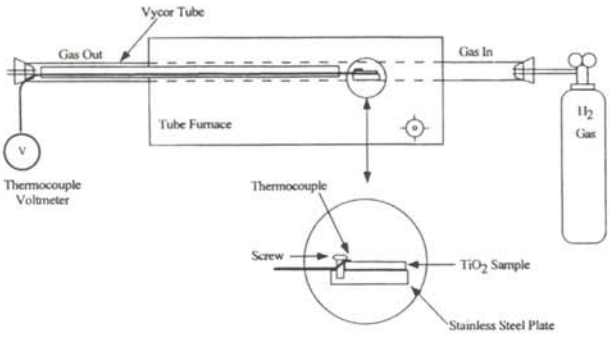


*Figure 1*
*Experimental set up for reduction of $TiO_2$ samples at 500 C in an oxygen poor environment.*

## THE EXPERIMENT

We began this research project by investigating the ability of $TiO_2$ to decompose water for applications in the solar evolution of $H_2$ gas, which can be used as a fuel and for direct production of electricity. The study of the surface morphology of the crystals, what we are reporting in this paper, arose as a side light to the intended purpose of this research.

When purchased, the $TiO_2$ crystal was transparent yellowish in appearance. One surface of the crystal was polished so that it is optically flat, variations over the entire surface do not exceed about 100 nm. Using an Atomic Force Microscope (AFM), we took images before and after reduction to see if the reduction produced any changes in the surface morphology of the crystal. A dramatic change was observed, which may be surface faceting, a result that has not yet been reported in samples reduced at 500 C.

Three single crystal wafers of rutile $TiO_2$ were used in this study, two cut along the (110) plane and one along the (001) plane. The samples measured 10 mm x 10 mm x 0.5 mm and were polished to optical flatness on one side. Each sample was imaged using the AFM before it was reduced. Several spots on each sample were examined to ensure that the surfaces were uniform.

Each sample was reduced in a tube furnace. Industrial grade hydrogen gas was passed at 10 p.s.i. through a Vycor tube, a type of glass tube made for use in extremely high temperatures, that was externally heated between 500 C and 550 C. The set up is shown in Figure 1. A calibrated chromel-alumel thermocouple attached to the sample holder measured the approximate sample temperature. The heating process was carried out until the transparent yellowish appearance of $TiO_2$ turned to a clear blue color, indicating that the sample was reduced from its insulating state to a semiconducting state. The reduced samples were again analyzed using the AFM, with images taken at various locations across the sample.

To further explore how morphological changes occur at this low reducing temperature, one of the (110) samples was only partially reduced. This gave insight as to whether the observed surface features can be attributed to the actual reduction process or whether they are the result of some other process that occurs curing heating.

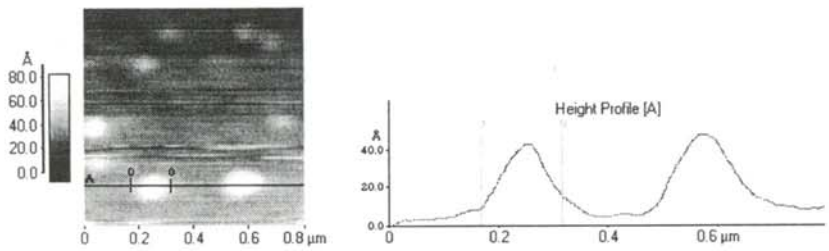


*Figure 2*
*$TiO_2$ (110) sample as received. The line profile shows the height of the small features, likely dust. The RMS roughness is 6.2 Å*

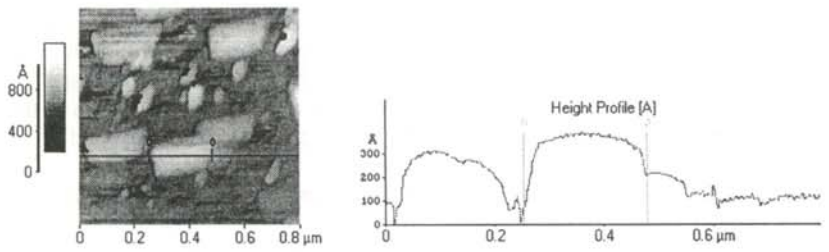


*Figure 3*
*$TiO_2$ sample after reduction. The large surface features are now evident. The RMS roughness is now 84 Å*

## DATA PRESENTATION and DISCUSSION

Figure 2 shows surface scan of a (110) sample before reduction. It has an average root mean square (RMS) roughness of 6.2 Å. The sample was then reduced for about 4 hours at 520 C with hydrogen gas flowing at 10 p.s.i. until it appeared transparent and bluish. Figure 3 shows the AFM image of this surface. Noticeable surfaces protrusions, likely facets, had formed. The mechanism that causes the formation of these features is presently not known. We speculate that the features are facets or regions of new crystal growth because of the regular shapes and sizes of these features. These features caused the RMS surface

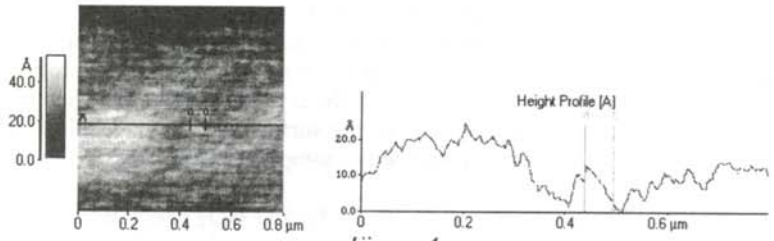


*Figure 4*

*Second $TiO_2$ (110) sample as received. This sample is slightly flatter than the first, with a RMS roughness is 4.0 Å.*

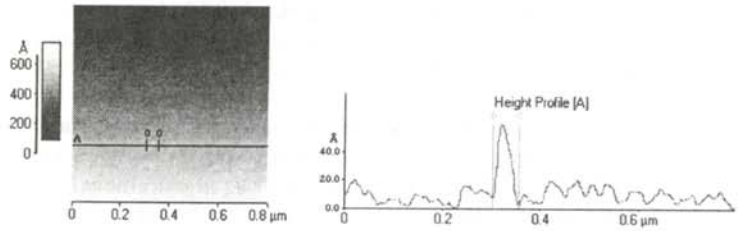


*Figure 5*

*Second $TiO_2$ (110) sample. This image is of a region that is only partially reduced. The RMS roughness is 7.6 Å, but no surface features are evident.*

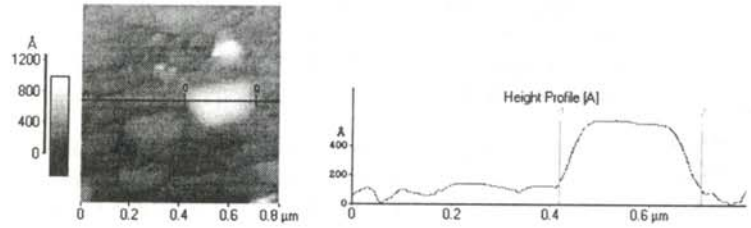


*Figure 6*

*Second $TiO_2$ (110) sample. This image is of a region that is completely reduced. The RMS roughness is 84 Å with surface features evident.*

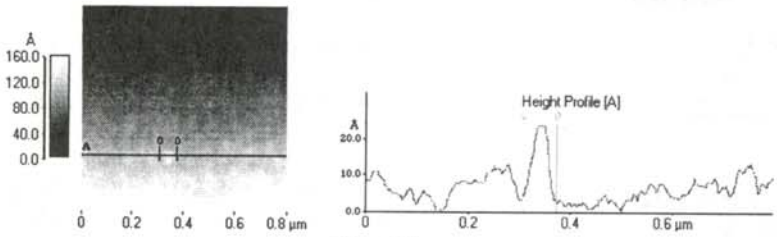


*Figure 7*

*Surface scan of $TiO_2$ (001) sample as received. The RMS roughness is 3.4 Å*

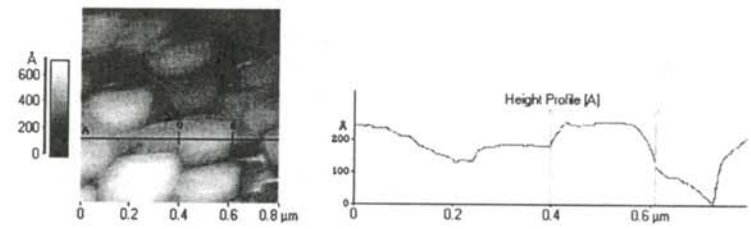


*Figure 8*

*Surface scan of $TiO_2$ (001) sample after reduction. The RMS roughness is 75 Å with surface features present. The features have different shape and density from those seen on the $TiO_2$ (110) sample.*

roughness to increase to 84 Å.

To check that these surface features were reproducible, a second sample with the (110) orientation was studied. Figure 4 shows the sample before reduction, with an RMS roughness of 4.0 Å. During reduction, the hydrogen gas was pressure was increased to 15 p.s.i. in an attempt to speed up the process. This higher pressure actually slowed down the reduction. After 4 hours, the sample still appeared to be some what yellow with some bluish color, indicating that the reduction was not complete. The surface of the sample was again imaged using the AFM. Figure 5 is an image of a light blue area which was only partially reduced. No noticeable surface features had formed. The average RMS roughness of the surface, 7.6 Å, indicated that the surface was a little rougher than the unheated surface, though this could be due just to variations in roughness across the sample. Figure 6, the image of a darker blue or fully reduced spot, shows some protrusions. The average RMS roughness of this area was 84 Å, the same roughness of the first (110) sample that was fully reduced. If some aspect of the heat treatment, such as a chemical reaction with hydrogen, were causing the features to form, they it should be seen uniformly across the sample. The process of reduction of the bulk sample creates the features on the sample surface.

The (001) orientation sample was studied to make certain that the "faceting" observed was not present in the (110) samples. Figure 7 shows the before reduction surface, showing an average roughness of 3.4 Å. The reduction process for this sample took only 3.25 hours with hydrogen gas flowing at about 8 psi. Figure 8 is the ATM image of the fully reduced sample. It shows many surface features and has an average RMS roughness of 75 Å. The (001) surface features are of different shape, size and density than those seen in the 110 samples. This supports faceting or crystal growth as being responsible for the observed features.

Our results suggest that the features we saw likely would occur on samples reduced even in a ultra high vacuum, a technique common in preparing samples for study of the properties of single crystal $TiO_2$ . We found that after reduction, the $TiO_2$ is no longer a single crystal. Consequently, reduced samples should not be used to study structure and properties of single crystal $TiO_2$ surfaces.

**ACKNOWLEDGMENTS**

The authors would like to acknowledge the agencies that supported their research. Brian Bradford was supported by the Colorado Alliance for Minority Participation (COAMP). John Kassay was funded by the Colorado Space Grant Consortium and by NASA.

**REFERENCES**

1. A. Fujishima, "The Raising of the Titanium", Look Japan, (June, 1995), pp. 26-27.
2. A. Fujishima and K. Honda, Nature, 238, (1972), pp. 37-38.
3. K.A. Davis, J. Chem. Ed., 59, 2, (1982), pp. 158-159.
4. R.V. Kasowski and R.H. Tait, Phys. Rev. B., 20, (1979), pp. 5178-5191.
5. J.B. Goodenough, "Metallic Oxides", Progress in Solid State Chemistry, Vol 5, Ed. H. Reiss, (Permagon), 1972.
6. L.E. Firment, Surface Science, 116, (1982) pp. 205-216.
7. Q. Zhong, J.M. Vohs and D.A. Bonnell, Surface Science, 274, (1992), pp. 35-43.

**FACULTY SPONSOR**

Dr. Ashley N. Shultz
Department of Physics and Engineering
Fort Lewis College
1000 Rim Drive
Durango, CO 81301
shultz_a@fortlewis.edu

# SOLVING THE OCTIC POTENTIAL PROBLEM USING THE VARIATIONAL METHOD

M. Wall* and D. Meidlinger†
Department of Physics
University of Nebraska at Omaha
Omaha, NE 68182-0266
received Sept. 3, 1997

**ABSTRACT**

In this work, we use three different types of trial wave functions: straight edged functions (triangular and trapezoidal); Lorentzian type; and Gaussian type functions to calculate the ground state and first excited state energies of the octic potential. We demonstrate that when using the variational method to study quantum mechanical bound state problems, we have the advantage of probing the characteristics of the problem without knowing the exact solution.

## INTRODUCTION

For most quantum mechanical problems, exact analytical solutions are difficult to obtain. When this is the case, many different methods are used to solve the problem. One of them is the variational method where solutions are constructed by making a "guess" based on the characteristics of the problem. For example, one may rely on the asymptotic behavior and the symmetry of the problem. Because of the necessity of choosing a good trial solution, this method depends heavily on physical insight and mathematical ability. It has the advantage, however, of providing an analytical form for the wave function which can be used in a variety of situations. [1,2]

In most quantum mechanical bound-state problems, one starts with the confinement potentials expanded in terms of a power series in $x$, where $x$ is the displacement or a generalized coordinate from the equilibrium position. The simplest problem involves taking the quadratic term, resulting in the well known and thoroughly studied harmonic oscillator. Mathematical difficulty arises when higher powers, such as the quartic and sextic terms are included. Many systematic studies using perturbational and variational methods have been done for the quartic and sextic anharmonic oscillators. [1,2,3] When the variational method [1,2] was used, several sets of trial wave forms were utilized to study the characteristics of the ground state and first excited state. The results show that guessing the correct asymptotic behavior for the trial wave functions will lead to more reliable results. We use a similar approach to investigate the scale-free octic potential well, whose quantum mechanical Hamiltonian is:

$$\hat{H} = -\frac{d^2}{dx^2} + x^8 \ . \qquad (1)$$

### *Why the Variational Method 4 works*

Instead of knowing the exact wave function $\Psi_o$ of the

*The project started when Marcel and Dave took quantum mechanics in the spring of 1995. Both participated in a Department of Energy Science and Engineering Research Semester (SERS) at the Oak Ridge National Laboratory. Dave visited the plasma division during the summer of 1995 and Marcel spent 8 months in the material science division in 1996. Our visits were so enjoyable that we decided to pursue careers in the areas of applied sciences.*

*Dave left UNO at his senior year and went to the Colorado School of Mines in Golden to get an Engineering Physics degree. He will graduate in the summer of 1998. The Navy's Nuclear Power school at Charleston, SC already has offered him an instructor position. He will be able to teach there and proceed with a Ph.D. degree in theoretical physics. Outside of class, Dave can be found either working in the optoelectronics division of NIST at Boulder, hiking the hills of Golden or practicing piano.*

*Marcel finished his senior project and graduated in the summer of 1997. He received a research assistantship from the Materials Science Department of the University of Illinois -Urbana-Champaign. Currently he is examining the surface/step interactions of the (001) and (111) faces of TiN grown by reactive magnetron sputtering using in situ STM and other surface characterization techniques. He is still taking courses and preparing for the qualifying exam. His free time is spent at home and playing volleyball.*

Hamiltonian, $\hat{H}$ , we use an approximation $\Psi$ which can be expressed as the linear combination of $\psi_n$, the $n^{th}$ exact wave function of the Hamiltonian. Based on the principle of superposition:

$$\Psi = \sum_{n=1}^{\infty} c_n \psi_n \ . \tag{2}$$

Since $\Psi_o$, $\Psi$ and $\psi_n$ are all normalized:

$$\sum_{n=1}^{\infty} |c_n|^2 = 1 \tag{3}$$

Using $\Psi$ to calculate the expectation value, $E$, of the Hamiltonian, $\hat{H}$ , we obtain:

$$E = \int_{-\infty}^{\infty} \Psi^* \hat{H} \Psi \, dV = \sum_{n=1}^{\infty} |c_n|^2 E_n \ . \tag{4}$$

Since the exact ground state energy, $E_o$, is less than the energy of the higher states, Equation 4 becomes for all $n$:

$$E \geq \sum_{n=1}^{\infty} |c_n|^2 E_0 \ . \tag{5}$$

Substituting Equation 3 into Equation 5 gives:

$$E \geq E_0 \ . \tag{6}$$

This result shows that the energy, $E$, given by the trial wave function, $\Psi$, is always greater than the exact energy, $E_o$.

A similar proof can be extended to the first excited state. As long as the trial wave function, $\Psi_1$, for the first excited state is orthogonal to the previously determined $\Psi_o$, the expectation value for $E_1$ from $\Psi_1$ is always greater than the exact value. This proof can be carried out to all excited states, but it is too tedious for higher excited states. Therefore, we restrict ourselves to the first two bound states.

To analyze how well the trial wave function was constructed, we write the trial wave function, $\Psi$, as the sum of the exact wave function plus some small error:

$$\Psi = \Psi_0 + \delta\Psi \ . \tag{7}$$

Writing Equation 2 in integral form and substituting Equation 7 into it and solving for $c_n$:

$$c_n = \int_{-\infty}^{\infty} \psi_n^* \Psi \, dV = \int_{-\infty}^{\infty} \psi_n^* \left(\Psi_0 + \delta\Psi\right) dV \ . \tag{8}$$

Since the ground state wave function, $\psi_0$ is orthogonal to all the excited state wave functions, $\psi_n$, we have:

$$\int_{-\infty}^{\infty} \psi_n^* \Psi_0 \, dV = 0 \ . \tag{9}$$

Therefore:

$$c_n = \int_{-\infty}^{\infty} \psi_n^* \left(\delta\Psi\right) dV \ , \text{for } n > 0 \tag{10}$$

If $\delta\Psi$ is small, the trial wave function is a good approximation. Based on Equation 10, all $c_n$'s other than $c_0$ will also be small. [5] Equation 5 then assures that $E$ will be very close to $E_0$.

By studying the familiar solutions to the harmonic oscillator problem, we deduce several essential features that are useful for constructing the trial wave functions for this problem. First, the bound state solutions are always localized around the origin, they decay rapidly when $x \to \pm\infty$. Second, there are two distinct groups of solutions, one that is symmetrical with respect to $x = 0$, $\{\Psi(-x) = \Psi(x)\}$, and the other that is antisymmetric, $\{\Psi(-x) = -\Psi(x)\}$. These two groups of wave functions are orthogonal to each other. We expect similar properties to continue for the solutions for higher order symmetrical potentials.

## CALCULATION AND DISCUSSION

Schrödinger's equation for our problem is:

$$-\frac{d^2\Psi}{dx^2} + x^8 \Psi = E \Psi \ . \tag{11}$$

For the first trial wave function, we use a single triangle wave function for the ground state (shown in Figure 1):

$$\Psi_0(x) = \begin{Bmatrix} 0 & |x| \geq \lambda \\ -\alpha(-\lambda + x) & \lambda \geq x \geq 0 \\ \alpha(\lambda + x) & 0 \geq x \geq -\lambda \end{Bmatrix}, \tag{12}$$

and a double triangle wave function, shown in Figure 2, for the first excited state:

$$\Psi_1(x) = \begin{Bmatrix} 0 & |x| \geq a \\ \gamma(x - a) & a \geq x \geq A \\ -\beta x & A \geq x \geq -A \\ \gamma(x + a) & -A \geq x \geq -a \end{Bmatrix}, \tag{13}$$

where continuity at $x = \pm A$ requires:

$$A = \frac{\gamma a}{\gamma + \beta} \ , \tag{14}$$

where $\alpha$, $\gamma$ and $\beta$ are the slopes and $a$ and $\lambda$ the $x$-axis intercepts of the edges of the triangles. Using the trail wave functions, Equations 12 and 13, we obtained the analytical expressions for the ground state and first excited state expectation values, which depend on the parameters $\alpha$, $\beta$, $\gamma$, $\lambda$, and a. Then, the energies can be optimized by using the International Mathematical Subroutine Library (IMSL) package. We utilized the routine UMINF in the optimization chapter 6 to find the minima of the total energies and, at the same time, all of the optimal values of the parameters.

Figures 1 and 2 show that $\Psi_0$ is symmetrical with respect to the $x = 0$ line while $\Psi_1$ is antisymmetric. This simple symmetry property makes $\Psi_0$ orthogonal to $\Psi_1$.

There are two advantages in using these triangular wave functions. First, they mimic the localized bound state wave functions, e.g. they resemble the ground and first excited wave functions of the harmonic oscillator. Second, they are quite easy to integrate. This is especially true for

the kinetic energy term, because it relates to the delta function. [1,2] After normalization, the expectation values can be calculated swiftly. The results depend only on one (for $\Psi_0$) or two (for $\Psi_1$) parameters.

We found ground a ground state energy, $E_0 = 1.43$ and a first excited state energy, $E_1$=5.49. Exact solutions to this problem can be obtained using a Runge-Kutta numerical integration program ($E_0 = 1.23$ and $E_1$= 4.76). This is a discrepancy of 16% and 15% respectively.

These results are good for such crude approximate wave functions. One problem that can be fixed the wave is the unphysical shape at the cusps. We can truncate the cusps and turn Equations 12 and 13 into the trapezoidal shapes. For the ground state (shown in Figure 1) :

$$\Psi_0(x) = \begin{cases} 0 & |x| \geq \beta \\ (x-\beta)\dfrac{a}{(\alpha-\beta)} & \beta \geq x \geq \alpha \\ a & \alpha \geq x \geq -\alpha \\ (x+\beta)\dfrac{a}{(-\alpha+\beta)} & -\alpha \geq x \geq -\beta \end{cases} . \qquad (15)$$

For the first excited state (shown in Figure 2):

$$\Psi_1(x) = \begin{cases} 0 & |x| \geq \beta \\ -\gamma(x-a) & a \geq x \geq B \\ a & B \geq x \geq A \\ -\beta x & A \geq x \geq -A \\ -b & -A \geq x \geq -B \\ -\gamma(x+a) & -B \geq x \geq -a \end{cases} , \qquad (16)$$

where:

$$A = \frac{b}{\beta} , \qquad (17)$$

and:

$$\beta = a - \frac{b}{\gamma} . \qquad (18)$$

The three optimization constants, $\alpha$, $\beta$ and $\gamma$ are found using the same techniques as before. The expectation values found for the trapezoidal trial wave functions are $E_0$=1.33 and $E_1$ = 1.12. The corrections improved the results, the discrepancies between the this technique and the Runge-Kutta results are 9.6% and 7.5%.

These examples show that the triangular wave functions are 'unphysical' at the cusps and that this discrepancy can partially be corrected by using the trapezoidal functions. However, the turning points of the wave functions are still not smooth. We could continue chopping off the sharp corners, but the wave function would become very complicated. Instead, we change to the continuous Gaussian type wave functions.

We chose the Gaussian type functions because: they are localized at $x = 0$ and are either symmetrical or antisymmetric with respect to the $y$ axis; they are differentiable to all orders, which implies a finite kinetic energy; they approach zero rapidly as $x$ tends to infinity (see Figure 3). This third characteristic is very important because we have to integrate the function from negative to positive infinity. The proper asymptotic behavior as $x$ approaches infinity is vital for the convergence of all the integrals.

Our first choice for the "true" Gaussian wave function for the ground state was:

$$\Psi_0 = N_0 e^{-\alpha x^2} , \qquad (19)$$

and for the first excited state (see Figure 4):

$$\Psi_1 = N_1 x e^{-\alpha x^2} , \qquad (20)$$

where $N_0$ and $N_1$ are normalization constants and $\alpha$ is the constant governing the width of the wave functions. Again, $\Psi_0$ and $\Psi_1$ are orthogonal to each other. We obtained energies of $E_0$=1.38 and $E$1=5.16, giving discrepancies of 12% and 8.3% respectively. To our surprise, these results were not as good as the answers obtained from the trapezoidal functions. We believe that the incorrect asymptotic behavior is responsible for the mediocre quality of the fit.

To test if the incorrect asymptotic behavior caused the problems, we adopted a modified Gaussian type wave functions:

$$\Psi_0 = N_0 e^{-\beta|x|^3} , \qquad (21)$$

and

$$\Psi_1 = N_1 x e^{-\beta|x|^3} . \qquad (22)$$

Even though Equations 21 and 22 are constructed to maintain the symmetry property of the wave functions, it is not difficult to check that these functions and their first and second derivatives are continuous at the origin. Again, $N_0$ and $N_1$ are the normalization constants and $\beta$ is the optimization constant used to find the minimum energy. This set of trail wave functions gave us the energies of $E_0$=1.2468 and $E_1$ = 4.7904. The discrepancies are greatly reduced; to 1.4% and 0.56% respectively. These are the closest results so far! We credit this accuracy to the correct asymptotic behavior of the trial wave functions.

We continued with Gaussian type wave functions for the ground state:

$$\Psi_0 = N_0 e^{-\alpha x^4} , \qquad (23)$$

and for the first excited state:

$$\Psi_1 = N_1 x e^{-\alpha x^4} , \qquad (24)$$

This time we found energy expectation values of $E_0$=1.32 and $E_1$=4.96. The discrepancies are 7.5% and 4.1% respectively. It appeared that the best results come from

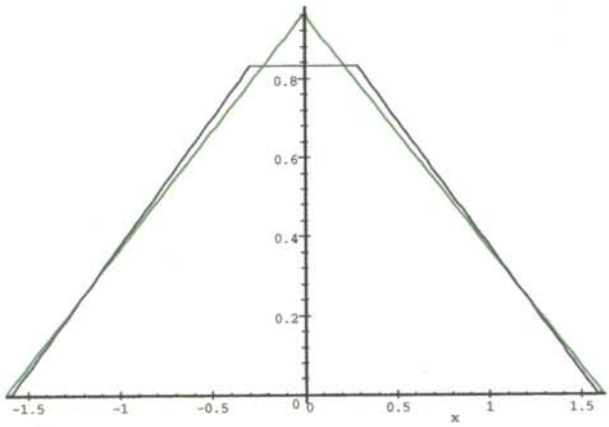


*Figure 1*
*Comparison of the two straight edged trial wave functions for the ground state: Equation 12 (red) and Equation 15 (blue)*

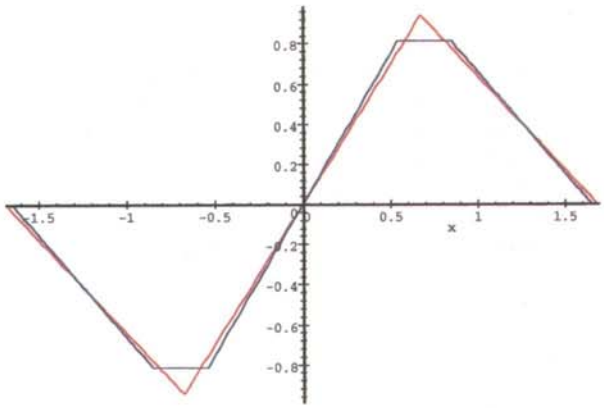


*Figure 2*
*Comparison of the two straight edge wave functions for the first excited state: Equation 13 (red) and Equation 16 (blue).*

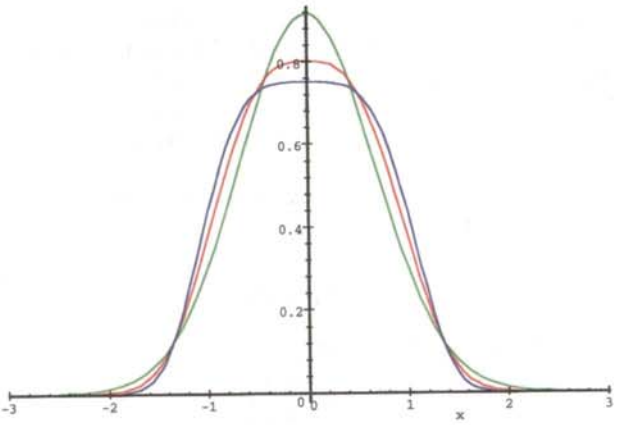


*Figure 3*
*Comparison of the Gaussian type trial wave functions for the ground state: Equation 19 (green), Equation 21 (red) and Equation 23 (blue).*

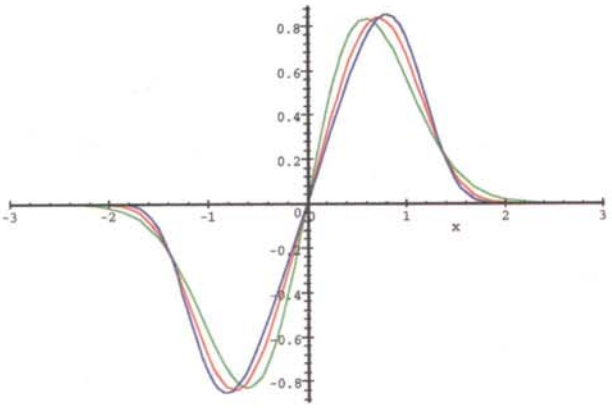


*Figure 4*
*Comparison of the Gaussian type trial wave function for the first excited state: Equation 20 (green), Equation 21 (red) and Equation 24 (blue)*

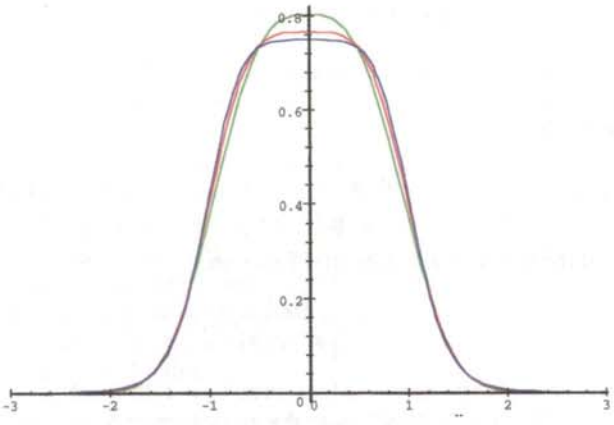


*Figure 5*
*Comparison of the Lorentzian type trial wave functions for the ground state: Equation 25 (green), Equation 27 (red) and Equation 29 (blue).*

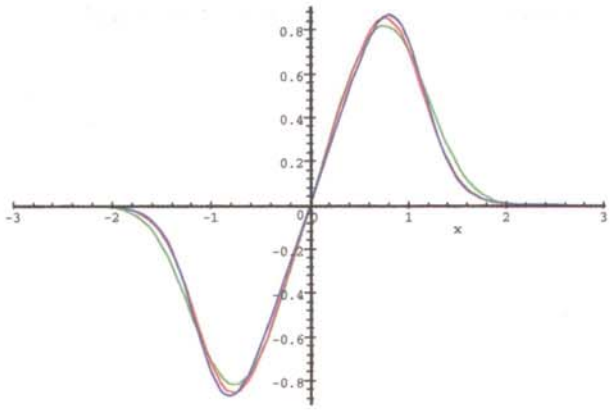


*Figure 6*
*Comparison of the Lorentzian type trial wave functions for the first excited state: Equation 26 (green), Equation 28 (red) and Equation 30 (blue).*

the Gaussian type functions in Equations 21 and 22.

Learning the asymptotic lesson from the previous work, we try a different group of trial functions, the Lorentzian type functions . They have many characteristics that are similar to the Gaussian type functions: they all have the smooth peak at $x = 0$ and that all approach zero rapidly as $x$ tends to $\pm\infty$ (see Figure 5). In addition, we can control the asymptotic behavior by varying the parameters $a$ and $n$, where $n$ is the power of the denominator.

The first Lorentzian type wave function we test was, for the ground state (see Figure 5):

$$\Psi_0 = \frac{N_0}{\left(|x|^3 + a^3\right)^n} , \qquad (25)$$

and for the first excited state (see Figure 6):

$$\Psi_1 = \frac{N_1 x}{\left(|x|^3 + a^3\right)^n} . \qquad (26)$$

where $N_0$ and $N_1$ are the normalization constants and $a$ and $n$ can be obtained by optimizing the expectation values of the Hamiltonian. All integrals involving the Lorentzian type wave functions are of the form: 7

$$\int_0^\infty \frac{x^{\mu-1}}{\left(p + q\,x^\nu\right)^{n+1}}\,dx =$$

$$\frac{1}{\nu\, p^{n+1}}\left(\frac{p}{q}\right)^{\mu/\nu}\frac{\Gamma\left(\frac{\mu}{\nu}\right)\Gamma\left(1+n-\frac{\mu}{\nu}\right)}{\Gamma(1+n)}, \text{ for } 0 < \frac{\mu}{\nu} < (n+1), \qquad (27)$$

where $\Gamma(x)$ is the Gamma function. With the trial wave functions of Equation 25 and 26, we find energy expectation values $E_0$=1.2467 when $n$ = 3480 and $E_1$ = 4.7904 when $n$ = 3328. These energies show discrepancies of 1.4% for the ground state and 0.56% for the first excited state. They are identical to the 4th digit to those obtained from using the wave functions of Equation 21 and 22.

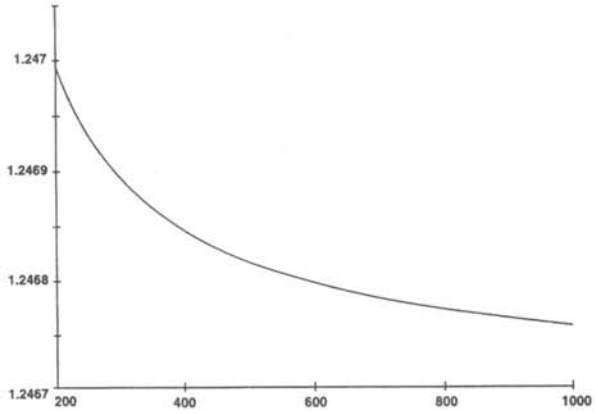


*Figure 7*
*Expectation value obtained using Equation 25 versus the exponent of the denominator, n.*

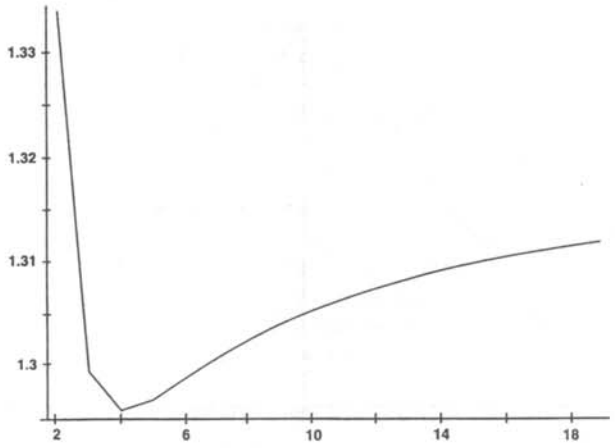


*Figure 8*
*Expectation value obtained using Equation 27 versus the exponent of the denominator, n.*

In Figure 7, we show how the ground state energy decreases as $n$ increases, but the rate of change with respect to $n$ is extremely small. We suspect that this may be a gradual confluence of the Lorentzian type function, Equation 25, into the Gaussian type function, Equation 21, but we are not going to prove it in mathematical rigor.

To improve the results, we continued using Lorentzian type ground state functions:

$$\Psi_0 = \frac{N_0}{\left(x^4 + a^4\right)^n} , \qquad (28)$$

and first excited state functions:

$$\Psi_1 = \frac{N_1 x}{\left(x^4 + a^4\right)^n} , \qquad (29)$$

where $N_0$ and $N_1$ are the normalization constants and $a$ and $n$ are optimization constants. The energies found were $E_0$ = 1.296 ($n$=4) and $E_1$ = 4.883 ($n$ = 5), resulting in discrepancies of 2.5% and 5.4% respectively. In Figure 8, we plot the ground state energy as a function of $n$. The minimum occurred at very small $n$.

To confirm that we reached the best results for the Lorentzian type function, we picked a trial ground state wave function:

$$\Psi_0 = \frac{N_0}{\left(|x|^5 + a^5\right)^n} , \qquad (30)$$

and the first excited state trial function:

$$\Psi_1 = \frac{N_1 x}{\left(|x|^5 + a^5\right)^n} , \qquad (31)$$

The energy expectation values were $E_0$ = 1.36 ($n$=2) and $E_1$ = 5.02 ($n$ = 3), resulting in discrepancies of 5.4% and 10% respectively. These values show that we reached the best trial wave function of this type.

Finally, two more complicated analytical wave functions

| Trial Wave function | Ground State Energy | Discrepancy % |
|---|---|---|
| *Runge-Kutta Numerical Solution* | 1.2258 | |
| *Straight Edged* | | |
| Equation 11 | 1.4306 | 11.4 |
| Equation 14 | 1.3347 | 9.61 |
| *Gaussian* | | |
| Equation 19 | 1.3801 | 12.3 |
| Equation 21 | 1.2468 | 1.41 |
| Equation 23 | 1.3216 | 7.50 |
| *Lorentzian* | | |
| Equation 25 | 1.2467 | 1.41 |
| Equation 28 | 1.2957 | 5.39 |
| Equation 30 | 1.3562 | 10.3 |

*Table 1*
*Ground state energy expectation values calculated using the various trial wave functions. The percentage discrepancy is a comparison to the numerical solution.*

| Trial Wave function | First Excited State Energy | Discrepancy % |
|---|---|---|
| *Runge-Kutta Numerical Solution* | 4.7559 | |
| *Straight Edged* | | |
| Equation 12 | 5.4947 | 15.3 |
| Equation 15 | 5.1208 | 7.49 |
| *Gaussian* | | |
| Equation 20 | 5.1577 | 8.27 |
| Equation 22 | 4.7904 | 0.55 |
| Equation 24 | 4.9585 | 4.08 |
| *Lorentzian* | | |
| Equation 26 | 4.7904 | 0.55 |
| Equation 29 | 4.8825 | 2.49 |
| Equation 31 | 5.0197 | 5.37 |

*Table 2*
*First excited state energy expectation values calculated using the various trial wave functions. The percentage discrepancy is a comparison to the numerical solution.*

which were used in the studies of the $x^4$ and $x^6$ potential [2] were included in the work for comparison. For the ground state:

$$\Psi_0 = N_0 \, e^{-\mu x^2 - \nu x^4} \, , \tag{32}$$

and for the first excited state:

$$\Psi_1 = N_1 \, x \, e^{-\mu x^2 - \nu x^4} \, , \tag{33}$$

were used as the trial wave functions. The energy expectation values were $E_0 = 1.229$ and $E_1 = 4.764$. Excellent agreement was found in comparison with the Runge-Kutta numerical integration method. However, the computations involved tedious integrals and lengthy numerical codes. [8]

Tables 1 and 2 are a summary of the numerical results of this investigation. The lessons we learned were that when working with the variational method one can always improve the results by probing thoroughly the characteristics of the problem. The solutions you get using the variational method may not necessarily be correct, but they certainly won't be wrong.

## ACKNOWLEDGMENTS

We would like to thank Dr. W.N. Mei for the guidance and ideas he gave us as we worked on our senior projects. We also thank Dr. D. Wilkins for his critical comments and careful reading of the manuscript. We gratefully acknowledge the teaching assistantship and financial support provided by the physics department of the University of Nebraska at Omaha.

## REFERENCES

* Current address of author: 811 Oakland Ave, Apt 3201, Urbana, IL 61801, mawall@students.uiuc.edu
† Current address of author: 16359 W. 10th Ave, #N2, Golden, CO 80401 dmeidlin@slates.mines.edu.

1. W.N. Mei, "Demonstration of the Systematic Improvements in the Application of the Variational Method to the Harmonic Oscillator", International Journal for Mathematical Education in Science and Technology, 27, (1996), pp. 285-292, are the references cited therein.
2. W.N. Mei, "Demonstration of the Systematic Improvements in the Application of the Variational Method to the Anharmonic Oscillator", International Journal for Mathematical Education in Science and Technology, 28, (1997), pp. 495-511, and the references cited therein.
3. E.J. Weniger, "A Convergent Renormalized Strong Coupling Perturbation Expansion for the Ground State Energy of the Quartic, Sextic and Octic Anharmonic Oscillator", Anals of Physics, 246, (1997), pp. 133-165.
4. D.A. Park, Introduction to the Quantum Theory, 3rd Ed, (McGraw Hill, Inc.), 1992 p. 241.
5. D.A. Park, *ibid.*, p. 242.
6. IMSL, 1989, Math/Library User's Manual, Chapt. 8, pp 783-937.
7. I.S. Gradshteyn and I.M. Ryzhik, Table of Integral Series and Products, (Academic Press), 19656, p. 292.
8. Due to the lengthy numerical codes needed to find the energy expectation values, the calculations were performed by Professor W.N. Mei of the University of Nebraska at Omaha.

## FACULTY SPONSOR

Dr. W.N. Mei
Department of Physics
University of Nebraska at Omaha
Omaha, NE 68182-0266
physmei@cwis.unomaha.edu

# A COMPUTER MODEL OF SOLAR SUPERGRANULATION

Dan Smith
Department of Physics
University of Nebraska at Omaha
Omaha, NE 68182
received Oct 1, 1997

**ABSTRACT**

We modeled, with several simplifying assumptions, a type of convective flow on the surface of the sun known as supergranulation. We checked our model against the real sun using the cross-correlation statistic. We found, using a special form of the cross-correlation known as the auto-correlation, that the supergranule velocity distribution used in our model is at least on the right track towards describing the actual velocity distribution within supergranules.

## INTRODUCTION

Convection occurs in the interior of the sun up to 2 x $10^5$ km below the photosphere. The convection cells come in different sizes and last for different lengths of time, The smallest cells, known as granules, are about 1 x $10^3$ km across and live for around 16 minutes. [1] Mesogranules are about 5 to 10 times larger [2] and live between 2 and 3 hours. [3] Supergranules, the subject of this study, are about 3 x $10^4$ km across and live for a day or longer. [4] Giant cells, the largest of these convection cells, are predicted theoretically and are expected to be about 5 times as large as supergranules. From time to time, claims of detecting structures like these appear. [5]

Gaseous flows on the surface of the sun can be observed using a telescope equipped with a spectroheliograph. [6] This device measures the speed of the gasses in the direction of the line of sight through the Doppler shifting of spectral lines. Figure 1 is a picture of the sun made with such an instrument. The blue colors represent velocities moving towards the observer, red colors represent velocities moving away and yellow represents zero velocity along the line of sight.

*Dan graduated Cum Laude from the University of Nebraska at Omaha in August, 1997 with a bachelor of science degree in mathematics and physics. In his senior year, he received the physics department's award as "Most Outstanding Student". He is planning to attend graduate specializing in Optics in the Fall of 1998. In his spare time, Dan enjoys running, biking, fencing and golf.*

The line-of-sight-velocity (LOSV) map of the sun, Figure 1, shows that much more is happening on in the sun than supergranulation. On the largest scale the color difference between eastern and western hemispheres, reflects the

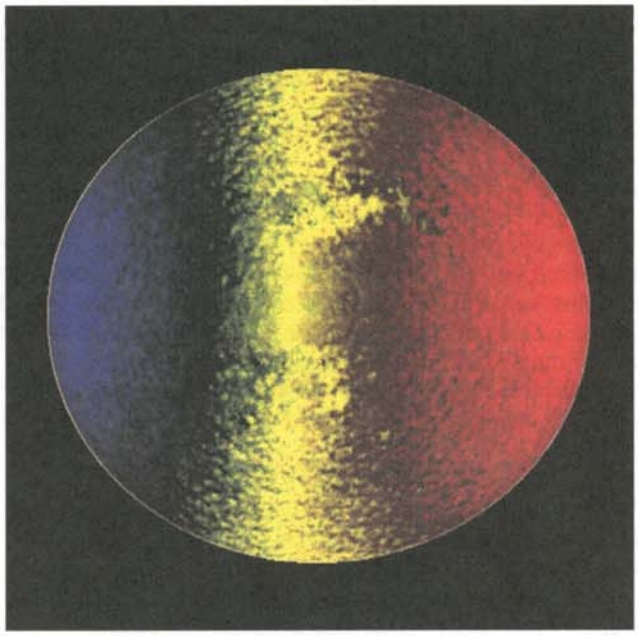

*Figure 1*
*Line-of-sight velocity map of the sun. Blue indicates motion towards the observer, red away from the observer and yellow represents zero velocity along the line of sight. The dominant feature shown here is the rotation of the sun about its axis. This is a Mt. Wilson image of the sun taken in July of 1988.*

Doppler shift associated with the sun's rotation. We used an algorithm that filters out the extraneous flows, such as the rotation of the sun, p-modes (five minute oscillations) and the gravitational redshift. [7] After applying this algorithm, a LOSV map such as the one shown in Figure 2 results. Maps such as Figure 2 serve as the standard against which we compare our simulated maps.

The solar disk in the LOSV map, shown in Figure 2, is not circular. This is the result of two manipulations: a change in coordinates; leaving off the outer 5% of the radius of the solar disk to avoid spurious effects which are the result of foreshortening on the solar limb. Each point on the surface of the sun can be designated by two variables: θ, the colatitude, the angle from the north pole; and ϕ, the azimuthal angle, measured from the positive x axis, as shown in Figure 3. Therefore, we can plot each point on the sun as a point on the Cartesian plane. This coordinate transformation alone would cause the map of the sun to appear rectangular in shape. The result of these two manipulations is a 'television screen' shaped sun. Large dark areas were masked out with 0's because they have magnetic fields large enough to compromise the measured Doppler velocities.

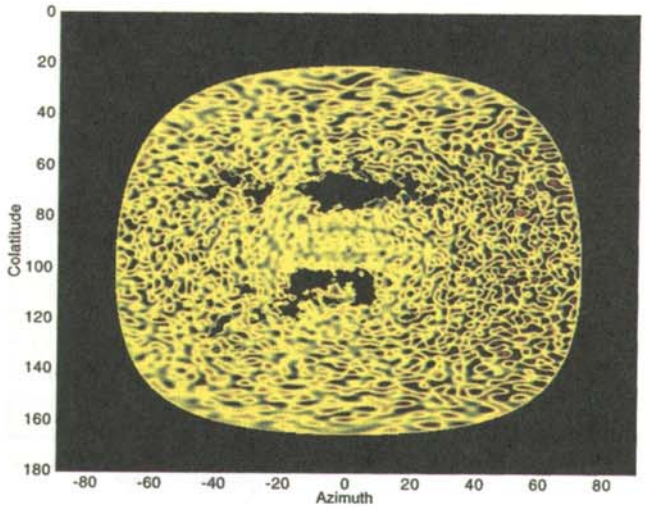


*Figure 2*
*The same sun as in Figure 1 after processing to remove the large scale features. The "television screen" shape is a result of removing the outer 5% of the solar radius and a change in coordinate system.*

## THE SIMULATION

Our model is based on an earlier work. [8] This model of a spherical, differentially rotating sun was originally written in FORTRAN. We chose Matlab™ as our developing platform because it has several advantages over the traditional languages such as FORTRAN or C. Matlab™ has an extensive, user-friendly, help facility. It is a high level language with many predefined functions which make data storage, imaging and other functions trivial. The greatest advantage of Matlab™ is that every variable is a matrix and contains fast, elegant ways of dealing with typical matrix and vector operations. This is particularly suited to our applications since we must generate and manipulate LOSV maps that are 512 by 512 matrices of pixel values.

### *Simplifying Assumptions*

Our model of supergranule activity in the sun is based on several assumptions. [9]

1) Supergranules are all identical. They live for the same length of time, have the same size, and are circular with well defined centers that are randomly and independently distributed over the surface of the sun.

2) Supergranules revolve about the sun at the same rate as the gasses of the photosphere. The rotational velocity, of the supergranules over the surface of the sun is given by the sidereal rate of rotation, Ω, which depends on the colatitude, θ, of the center of the supergranule:

$$\Omega = \left\{ 14.44 - 1.98 \left[ \cos^2(\theta) + \cos^4(\theta) \right] \right\} \frac{degrees}{day}. \qquad (1)$$

3) Supergranules do not evolve much over time. They are born, mature quickly and die quickly. [10]

4) At any particular time, the total number of supergranules 'alive' on the sun is relatively constant. To accomplish this, we introduce the concept of the supergranule family. A time of one 'generation gap', $g$, after the death of a parent supergranule, a daughter supergranule is born. This new supergranule lives for a specific period of time (two half lives - $2\tau$) and then dies. One generation gap later, another supergranule is born. If there are $N_{sf}$ supergranule families, the average number of 'living' supergranules on the sun at any particular time will be:

$$\langle N \rangle = N_{sf} \frac{2\tau}{g + 2\tau}. \qquad (2)$$

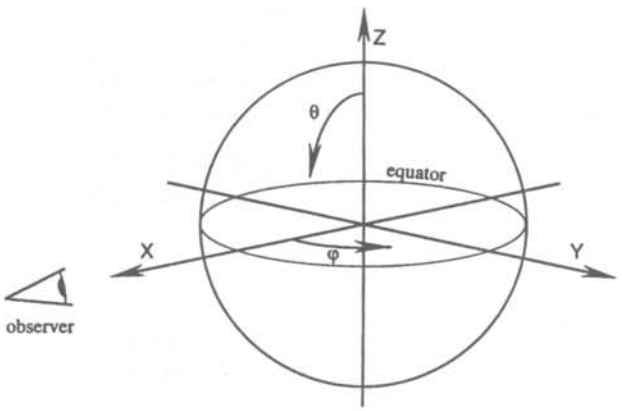


*Figure 3*
*Coordinate system used in our model of the sun.*

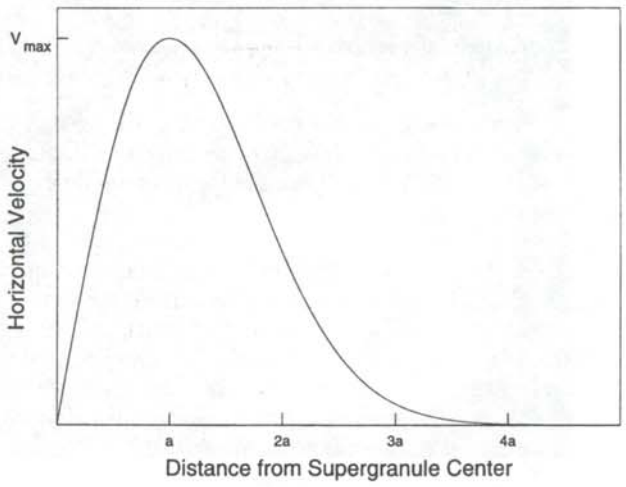


*Figure 4*
*A plot of the horizontal velocity vs distance from the center of the supergranule (from Equation 3).*

The birth time of the first supergranule in each family is random, but subsequent generations in each family appear with clocklike regularity with a period of $2\tau + g$.

To prevent an exact repetition of our model sun every generation, the birth location of the daughter is placed at a random position within a circular birth zone whose radius increases with the square root of the time after death. The birth zone is centered on the position that the parent would have reached if it had continued to revolve around the sun's axis after its death.

5) The predominant flow of gases in supergranules is parallel to the surface of the sun, with peak speeds between 300 m/s to 500 m/s. Vertical velocities, perpendicular to the surface of the sun are much smaller, except at cell boundaries, where significant down drafts exist. [11] The horizontal velocity is a function of the distance, $r$, from the center of the supergranule: [12]

$$V_{hor} = V_{\max} \frac{r}{a} \exp\left[\frac{(a^2 - r^2)}{2a^2}\right]. \qquad (3)$$

Figure 4 is a plot of Equation 3. Note that the horizontal velocity reaches its maximum at the scale radius $r = a$.

6) The supergranules are independent of each other, they do not interact. When the supergranules overlap, their velocity fields add vectorially.

## THE ALGORITHM

### *Generating Supergranule Histories*

Since each supergranule lives for a time twice the half life and travels along a path of constant colatitude at a speed given by Equation 1, the position of any supergranule at any time can be determined if we track its mid-life time and position. Three matrices are created that contain for each family (column) and for each generation (row) the mid-life properties: time, central $\theta$ and central $\phi$. This is done in three steps:

- The user inputs the number of supergranule families.

- Random mid-life times for the first generation of each family between $-\tau$ and $\tau + g$ are generated. From this, successive mid-life times are generated in increments of $2\tau+g$ until a specified final time.[13]

- Random positions for the first generation of each family are created. To ensure a uniform distribution over the surface of the sun, a random $\cos(\theta)$ and a random $\phi$ are generated. A randomly chosen $\theta$ and $\phi$ would overpopulate the poles. [14] Using these initial positions and the values of $t$, $g$ and a specified random walk coefficient, $C$, random birth positions are generated within birth zones of radius, $r_{bz}$:

$$r_{bz} = C\sqrt{g}\,, \qquad (4)$$

and azimuthal angle, $\varphi_{bz}$ :

$$\varphi_{bz} = g\,\Omega(\theta_{parent}) \qquad (5)$$

from the death position of the parent.

### *Generating the LOSV Map*

After generating the mid-life times and positions of the supergranules, we use Equation 3 to create model LOSV maps, analogous to Figure 1, of the surface of the sun. We determine an 'observation time' at which we would like to generate a map. Then we determine which supergranules

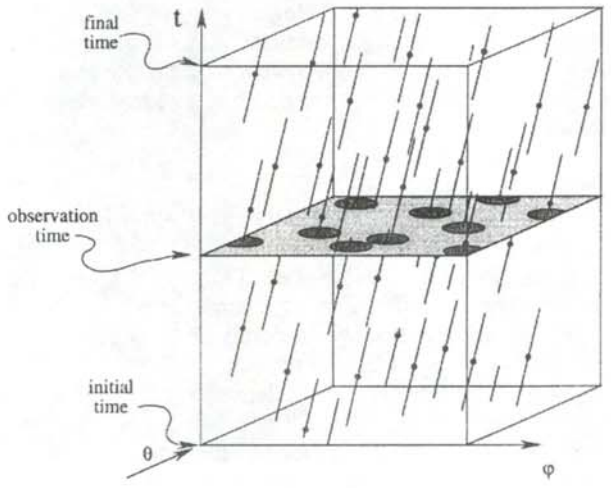


*Figure 5*
*Three dimensional history of supergranulation with time along the vertical axis, the azimuth angle along the horizontal and the colatitude angle into the page. To simplify the diagram, differential rotation is ignored, so the tilt of each line is the same. The "TV mask" is omitted.*

are alive at this time (called the contributing supergranules).

The history of the supergranules is visualized in three dimensions: $\theta$, $\phi$ and time. Figure 5 is a representation of the history of the supergranule centers as they move through time along constant colatitudes. [15] Their centers trace out paths of equal duration. A dot at the center of each path represents mid-life. At a particular observation time, the generated map can be represented as a plane parallel to the $\theta$–$\phi$ axes. The disks about the points where the line segments pierce the plane represent the limiting radii ( $r \leq 4a$) within which the supergranules make a non-negligible contribution to the line-of-sight-velocity. To simplify the diagram, differential rotation is ignored, so the tilt of each line is the same and the "TV mask" is omitted.

At a given observation time, each family of supergranules can contribute at most one live supergranule. Therefore, contributing supergranules are located by looping through each family's mid-life times to determine which ones are alive at the particular observation time. Simultaneously, the corresponding positions at the observation time are calculated from the mid-life positions using Equation 1. These positions are stored in two separate arrays used in generating the LOSV map.

The positions of the supergranule centers are transformed into pixel locations on our 512 x 512 matrix. To find the $\theta$ and $\phi$ values for the center of a pixel location *(i,j)* we use:

$$\varphi = \left(i - \frac{1}{2}\right)\frac{\pi}{512} - \frac{\pi}{2}$$
$$\theta = \left(j - \frac{1}{2}\right)\frac{\pi}{512} \quad . \qquad (6)$$

We subtracted $\pi/2$ from $\phi$ since we are looking at the sun antiparallel to the x-axis and, by convention, the 'prime meridian' ($\phi = 0$), must cut the solar disk in half.

Examination of Figure 4 shows that when $r = 4a$, $V_{hor} \approx 0$. This defines the edge of the supergranule. Using this condition and Equation 6, we loop through the pixels affected by each contributing supergranule and calculate the LOSV due to that supergranule using Equation 3. Appendix 1 contains the derivation of the LOSV at a point on the sun due to the horizontal velocity of a supergranule. Using the results shown in Appendix 1, we generated LOSV maps. Figure 6 is an example of one such calculation. As in Figures 1 and 2, blue colors represent velocities directed towards the observer and red represents velocities directed away

## TESTING THE MODEL

Cross-correlation is a measure of the similarity between two ordered sets of equal length. The discrete version of the cross-correlation is:

$$Cross\ Correlation = \frac{\sum_i \left(v_i v_i'\right)}{\sqrt{\sum_j v_j^{2}}\sqrt{\sum_k v_k'^{2}}}, \qquad (7)$$

where v and v′ are the members of the sets. We use the cross-correlation to compare horizontal strips of colatitude across pairs of LOSV maps generated at a certain time apart (called the lag time).

Imagine two LOSV maps generated at some lag time apart, the earlier map lying on top of the later one. If the top map is slid some distance (the azimuthal shift), we can calculate the cross-correlation on an overlapping strip of colatitude. The cross-correlation is expected to reach a maximum when the azimuthal shift is equal to the sidereal rate of rotation (Equation 1) times the lag time.

We used a special case of the cross-correlation of thin bands along the equator where the lag time is zero to analyze our results. This technique compares one map to itself and is properly called the auto-correlation. The shape of the auto-correlation should depend heavily n the size and the velocity distribution of the supergranules. Figure 7 is a plot of the auto-correlation for both the real sun and our model sun. Each curve is averaged over many maps.

The large negative dip in each curve of Figure 7, at a lag distance of about 3 degrees, is a result of the circular symmetry of the supergranules. The similarity of the curves shows that the Simon-Weiss velocity distribution that was used in our model is at least on the right track. The fact that the depth of the first dip in the auto-correlation for the real sun is not as deep as that of the model may be due to unfiltered noise in the real sun LOSV maps, random non-symmetries in the shapes of the real supergranules or differences between the theoretical velocity distribution and the actual velocity distribution, or most probably, a combination of these.

In the future, further analysis of the cross-correlations may give insight into the rotation, life time, size and other properties of supergranules. The model can serve as a tool for comparison between the theoretical and the observed.

## ACKNOWLEDGMENTS

The author wishes to acknowledge the previous work and assistance of Marcel Wall, Stuart Harman, Dr. D. Wilkins, Dr. J. Kasher, Dr. D.H. Hathaway and, in particular, Terry Hrabik whose handwritten manuscript regarding the original program was critical in the creation of this model. The project was supported by the University of Nebraska at Omaha Department of Physics and the NASA Nebraska Space Grant and EPSCoR programs.

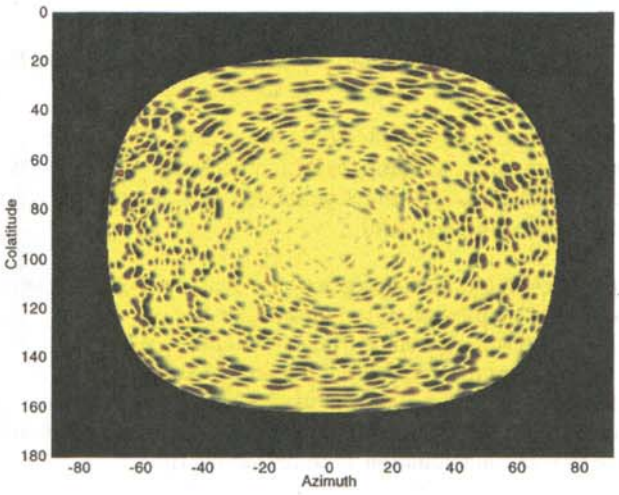


*Figure 6*
*Line-of-sight velocity map of the model sun, analogous to Figure 2. It has roughly 360 visible supergranules within the 95% radius "TV screen". The colors again reflect the relative motion of the supergranules.*

## APPENDIX 1

***LOSV derivation*** [16]

The coordinates of the supergranule center $(\theta_c,\phi_c)$ and the center of the pixel $(\theta_p,\phi_p)$ can be transformed into Cartesian coordinates as:

$$\begin{aligned} r_{center} &= (x_c, y_c, z_c) & r_{pixel} &= (x_p, y_p, z_p) \\ x_c &= r_{sun}\sin(\theta_c)\cos(\varphi_c) & x_p &= r_{sun}\sin(\theta_p)\cos(\varphi_p) \\ y_c &= r_{sun}\sin(\theta_c)\sin(\varphi_c) & y_p &= r_{sun}\sin(\theta_p)\sin(\varphi_p) \\ z_c &= r_{sun}\cos(\varphi_c) & z_p &= r_{sun}\cos(\varphi_p)\,. \end{aligned} \tag{8}$$

The distance, r, between the two positions is: [17]

$$r = r_{sun}\cos^{-1}\left[\vec{r}_{center}\cdot\vec{r}_{pixel}\right]. \tag{9}$$

The distance found by Equation 9 is used to calculate the horizontal velocity using Equation 3.

To determine the LOSV, we need to compensate for the tilt of the sun, $B_o = 7.25^\circ$, from the plane of the earth's orbit. This is done by a rotation of axes by an angle $B_o$. The pixel and supergranule center location in the rotated (primed) coordinate system is:

$$\vec{r}' = \begin{bmatrix} \cos(B_o) & 0 & -\sin(B_o) \\ 0 & 1 & 0 \\ \sin(B_o) & 0 & \cos(B_o) \end{bmatrix} \vec{r}\,. \tag{10}$$

The line-of-sight component of the horizontal velocity is found by multiplying the horizontal speed by the x-component of the unit vector in the direction of the horizontal velocity. To find that unit vector, we take the cross product of the rotated supergranule center vector and the rotated pixel vector and then take the cross product of that and the rotated pixel vector again:

$$\vec{N} = (\vec{r}'_{center}\times\vec{r}'_{pixel})\times\vec{r}'_{pixel} \tag{11}$$

The normalized x-component is found by dividing the x component of Equation 11 by the magnitude of Equation 11:

$$U_x = \frac{N_x}{\sqrt{\vec{N}\cdot\vec{N}}}\,. \tag{12}$$

Equation 12 is multiplied by the horizontal velocity (Equation 3) to get the LOSV:

$$V_{los} = -U_x V_{hor}\,. \tag{13}$$

## REFERENCES


1. R.J. Bray. R.E. Loughhead and C.J. Durrant, The Solar Granulation, 2nd Ed, (Cambridge University Press), 1984, Table 2.13, P. 93.
2. G.W. Simon and N.O. Weiss, Apl. J., 345, (1989), p. 1060.
3. L.J. November, J. Toomre and K.B. Gibbie, Apl. J., 245, (1981), p. L123, and Muller *et. al.*, Nature, 356, (1992), P. 322.
4. R.J. Bray and R.E. Loughhead and C.J. Durrant, *ibid.*
5. D.E. Thomsen., Sci. News, 127, (May 25, 1985), p. 326.
6. R.B. Leighton, R.W. Noyes and B.W. Simon, Apl. J., 135, (1962), pp. 474-499.
7. D.H. Hathaway, Solar Phys., 108, (1987), p. 1 and D.H. Hathaway, Solar Phys., 137, (1992), p. 15.
8. In the summer of 1993, Terry Hrabik and Stuart Harman began with a planar "toy model" suggested by


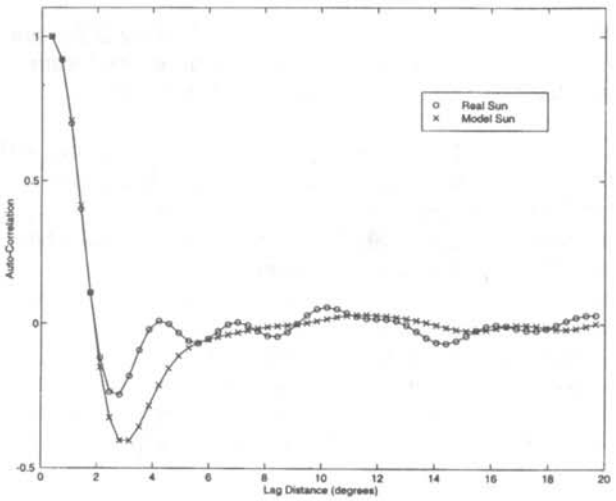


*Figure 7*
*Auto-correlation vs the lag distance when the lag time is zero. The crosses are for the model sun and the circles represent the correlation for the actual sun. Each set of data represents averages over several maps and over a 10 degree band along the equator.*

Dr. Dan Wilkins. They soon developed and implemented a more realistic model based on a spherical, differentially rotating sun. The code for this model was written in FORTRAN.

9. S. Harman, T. Hrabik, J. Kasher, D. Smith and D. Wilkins, "A Simon-Weiss Model for Supergranule Flows and their Cross-Correlations", submitted to Solar Physics.
10. E.G. Gibson, The Quiet Sun, (NASA, Washington), 1973, sp-303.
11. R.J. Bray, R.E. Loughhead and C.J Durrant, *Ibid.*
12. G.W. Simon and N.O Weiss, *Ibid.*
13. Actually, we generate successive mid-life positions a distance of $(2\tau+g)\ \Omega(\theta_p)$ from the parent mid-life position using the same birth zone radius.
14. This can be seen from the differential piece of area $d(\cos\theta)\ d\phi = \sin\theta\ d\theta\ d\phi$.
15. This diagram was originally conceived by T. Hrabik in his manuscript.
16. In developing the MATLAB program, many key equations were derived from a manuscript written by Terry Hrabik.
17. The original Harman-Hrabik FORTRAN program, used the straight line distance. We have chosen the arc length for its simplicity, although the actual difference is very small.

**FACULTY SPONSOR**

Dr. Dan Wilkins
Department of Physics
University of Nebraska at Omaha
Omaha, NE 68182-0266
wilkins@unomaha.edu

# DIFFRACTION PATTERNS OF LIGHT FROM HELICAL OBJECTS: Measurement and Calculation.

J.D. Levy*
Department of Physics
Hope College
Holland, MI 49423
received Jan 20, 1998

**ABSTRACT**

A Helium-Neon laser was used to study the diffraction patterns of helical objects in an upper-level undergraduate laboratory experiment. The presence of such objects in a variety of applications, from biology to manufacturing, and their distinctive diffraction patterns make them ideal candidates for illustrating the principles of diffraction in a laboratory. Predicted correlations between the patterns and diameter, pitch and coil angle were verified. The experiment also provides opportunities for introducing and using numerical Fourier transform techniques.

## INTRODUCTION

Almost all physics students are familiar with the standard examples of diffraction presented in the introductory courses: diffraction by one or two slits, or by a circular aperture. Unfortunately, the simplicity of the objects producing the diffraction patterns fails to demonstrate the more general principles of Fraunhofer diffraction. Essentially helical objects, such as screws and springs, are examples of nontrivial shapes that produce interesting diffraction patterns when illuminated by coherent light. A study of the diffraction patterns produced by these shapes is an excellent advanced laboratory experiment.

Light diffraction by helical objects has applications in a number of fields. The patterns provide vital clues that helped identify the helical structure of DNA in the 1950's.[1] In a manufacturing setting, diffraction patterns help provide automatic production control of screws and other small pieces.[2-4] Surprisingly, the literature is surprisingly deficient in this area. We were unable to find discussions of the topic in any standard optics textbook or journal in the English language. The idea for this experiment was taken from a book by R.S. Sirohi.[5]

*Joshua Levey developed this laboratory as a junior at Hope College, where he studied physics, computer science and mathematics. He now continues his studies under an NSF Graduate Fellowship in mathematics at the University of California, Berkeley.*

## MODELING DIFFRACTION

When a coherent light source illuminates an aperture, a Fraunhofer diffraction pattern of the aperture is formed at infinity. If the geometry of the aperture $A$ is described by the function $t(x,y)$, where $t(x,y) = 1$ for points where the light is transmitted through the object and $t(x,y) = 0$ elsewhere, the amplitude distribution at each point of the Fraunhofer image is proportional to the integral:

$$\iint_A t(x,y)\, e^{ik(px+qy)}\, dx\, dy \quad , \qquad (1)$$

where $p$ and $q$ are the direction cosines of the image point and $k$ is the wavenumber of the light. The light intensity of the image is given by a two-dimensional Fourier transform of the shape of the aperture. A more detailed description of this can be found in standard optics texts.[6]

We find the diffraction pattern numerically by using a two-dimensional fast Fourier transform (FFT) algorithm to perform the necessary convolution. FFT's can be computed by a variety of means. Computer program packages such as Matlab™ 7 will calculate the FFT's. If the student wishes to write a program to do the FFT, algorithms and discussions can be found elsewhere.[8] We used a freely available FFT program[9] that does efficient computation and requires only small amounts of additional programming to facilitate reading and writing the data.

The completed program calculated a grey-scale image of the diffraction pattern of any aperture, stored as an array of roughly one thousand by one thousand pixels. The apertures were defined using a drawing program [10] and the output written in a standard format readable by the FFT program. For example, Figure 1(a) shows a circular

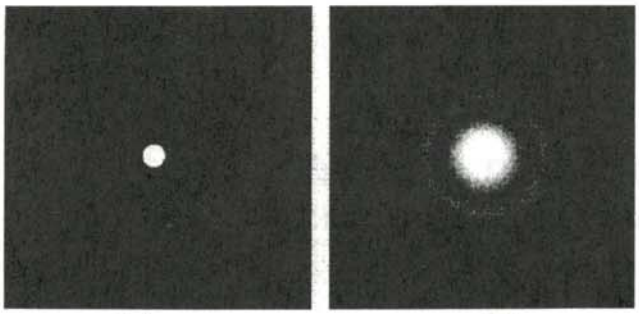

(a) (b)

*Figure 1*
*A circular aperture (a) and its computed Fraunhofer diffraction pattern (b).*

aperture and Figure 1(b) is the calculated transform, showing the familiar concentric rings of the Airy diffraction pattern. Since the coloring of the output image is a function of the logarithm of the intensity, small irregularities introduced by aliasing effects in the FFT were apparent in some places. The calculations for grids of such size took only a few seconds on a Sun SPARCstation 20. If computer resources are scarce, smaller grids can be used.

Our goal was to study objects in the general shape of a screw, having an opaque silhouette of the form shown in Figure 2(a). The diffraction pattern produced when coherent light illuminates the screw forms the general shape of an X, as shown in Figure 2(b). Sirohi [5] gives an analytical expression for the light intensity at the focal plane. Figure 3 shows the details of the object and the corresponding diffraction pattern. Note the following characteristics:

- The horizontal spacing of the intensity maxima is inversely proportional to the diameter of the screw: $d \propto 1/D$.
- The vertical spacing of the intensity maxima is inversely proportional to the spacing between the threads of the screw: $p \propto 1/P$.
- The angle between the diagonal lines on the X of the diffraction pattern is the same as the thread angle $\alpha$.

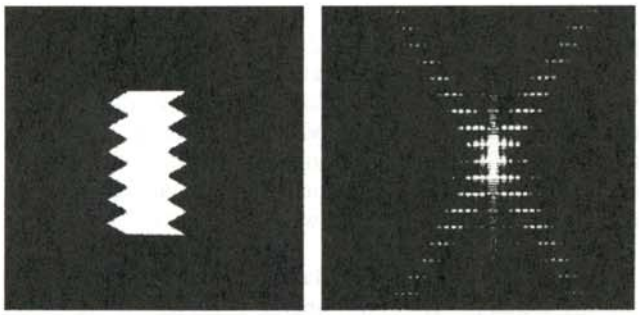

(a) (b)

*Figure 2*
*The outline of a typical screw (a) and its computed Fraunhofer diffraction pattern (b).*

## EXPERIMENTAL PROCEDURE

All that is needed to produce the diffraction is a Helium-Neon laser, some simple optical equipment and a variety of small helically shaped objects, such as screws or springs. In principle, it is sufficient to illuminate the object with the laser and focus the beam onto a screen with a converging lens. However, the patterns are best seen if a few additions to this system are made.

Figure 4 shows an experimental layout that we found to be effective. The beam, originating at the laser (1), is expanded to about 3 cm in diameter and collimated (2). Any extraneous light is caught by the mast (3) before interacting with the object (4). If the beam were now focused directly onto the screen, the central bright spot of the pattern would "drown out" the more faint pattern we wish to see. To eliminate the central bright spot, the converging lens (5) focuses the light onto a string crosshair (6), that blocks the light passing directly through the center and along the horizontal and vertical axes. Following the crosshair, converging (7) and diverging (8) lenses are used to refocus the beam onto the screen. The size and focal point of the emage can be adjusted by moving lenses 7 and 8.

The crosshair can be adjusted (or removed) to block any part (or none) of the pattern. For instance, if the screw is mounted on a horizontal base, the line of the base creates a bright vertical line through the center of the pattern. This can be blocked by the vertical string of the crosshair, allowing the other features of the pattern to be seen better.

The screen (9) is white cardboard or, if photographs are desired, a ground glass plate. Cardboard shields are used at several stages to mask any stray light, keeping it from reaching the screen. Table 1 lists the properties of the lenses we used in our experiment.

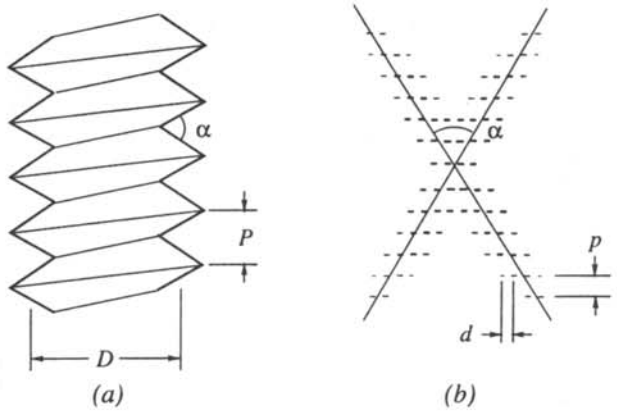


(a) (b)

*Figure 3*
*Schematic diagram showing the relationship between the screw parameters (a) and the diffraction pattern (b): $p \propto 1/P$ and $d \propto 1/D$.*

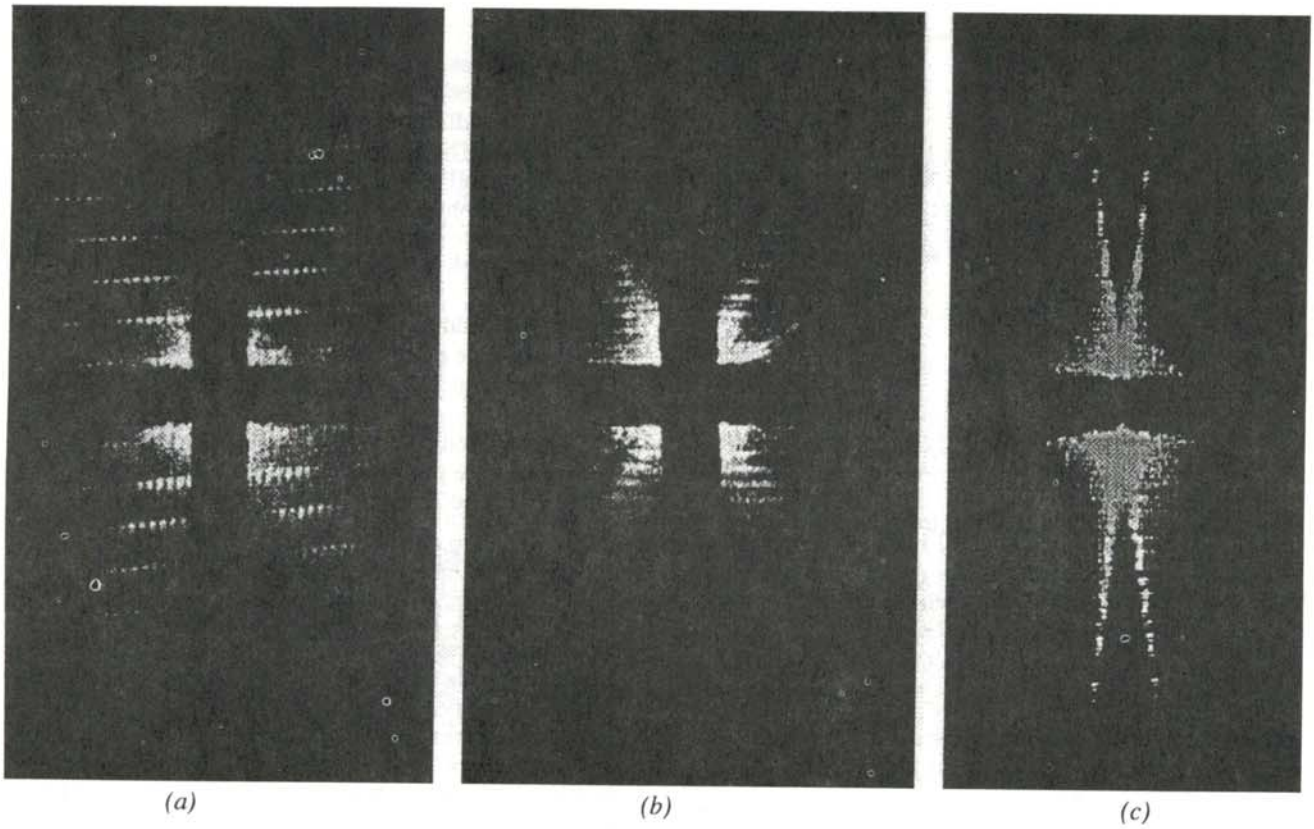

(a) (b) (c)

*Figure 5*
*Diffraction patterns produced by (a) a 2-56 screw, (b) a 1/4-20 screw and (c) the spring from a ball point pen.*

## RESULTS

We obtained diffraction patterns produced by a number of screws and springs. In each case, a pattern of the form shown in Figure 2(b) was obtained. Figure 5 shows some typical results. Figure 5(a) the pattern produced by a standard 2-56 screw. Figure 5(b) is the pattern produced by a 1/4-20 screw. Figure 5(c) is the pattern produced when the laser light was diffracted by the spring removed from an inexpensive ball-point pen. The angle between the diagonals of the X in Figure 5 was within two degrees of the true value for each object. (It is useful to know that the standard thread angle for the standard American machine screw is 60 degrees. )

To demonstrate the effect of diameter and thread pitch on the diffraction pattern, the patterns of six screws of various sizes were photographed and measured. Figure 6 shows the number of bright spots per unit of horizontal distance for the pattern produced by each screw as a function of its diameter. Given the uncertainties of the photographic measurements, the least-squares regression line matches the data well, and passes almost exactly through the origin. This is evidence that the horizontal spacing between maxima in the intensity pattern is inversely proportional to the diameter of the screw, just as it would be for a smooth rod. The inverse relationship between the screw pitch and the vertical spacing of the diffraction pattern is demonstrated in a similar fashion in Figure 7.

The parameters of the screw can be measured directly from the pattern dimensions. It has been suggested [5] to use the diffraction patterns to spot errors in a production line setting. Other patterns also can be studied. The ease in the drawing of apertures and the calculation of the

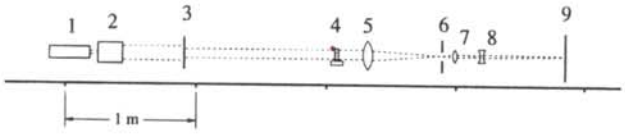


*Figure 4*
*Layout of the optical elements for obtaining diffraction patterns.*

| Lens | Focal length | Diameter |
|---|---|---|
| 5 | 42 cm | 3 cm |
| 7 | 16 cm | 2 cm |
| 8 | -6 cm | 1 cm |

*Table 1*
*Lenses used in Figure 4.*

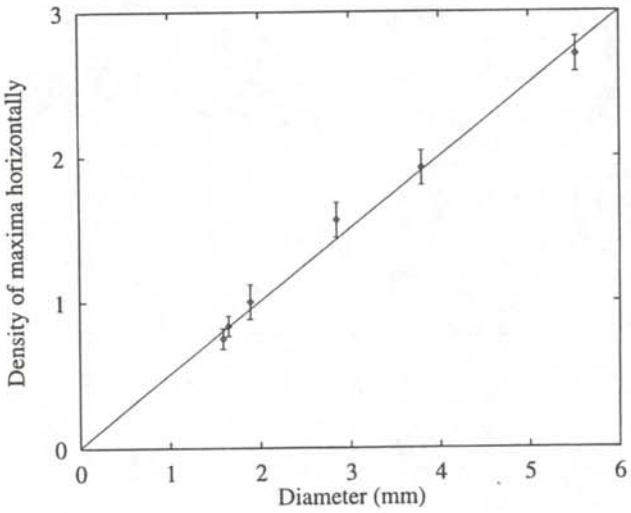


*Figure 6*
*Number of maxima in the diffraction pattern per arbitrary unit of width as a function of screw diameter.*

diffraction patterns produced by the apertures makes possible a search for new shapes that have interesting-looking diffraction patterns.

This diffraction experiment in an ideal way of applying the concepts of Fourier transforms to a real system. The computational aspect of the experiment gives a practical experience in using FFT's and gives an intuitive "feel" for Fourier transforms. The simplicity of the apparatus allows the student to focus on the diffraction patterns without spending too much time on experimental details.

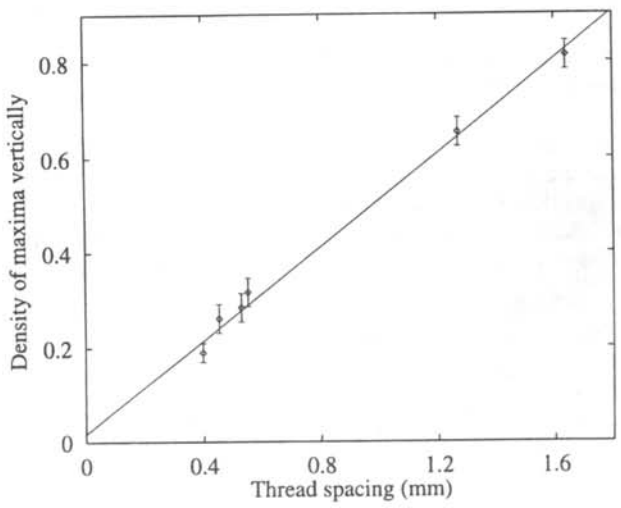


*Figure 7*
*Number of maxima in the diffraction pattern per arbitrary unit of height as a function of screw thread pitch.*

## REFERENCES

* Current address of the author: Department of Mathematics, University of California at Berkeley, Berkeley, CA 94720. jdl2@math.berkeley.edu

1. Robert Olby, The Path to the Double Helix, (University of Washington Press), 1974, and references therein.
2. J. Steffen, "Kontrolle von automatischen Frabikationsprozessen mith holographischen Verfaren", Feinwerktechnic & Messtechnik, 85(4), (1977), pp. 141-150.
3. J. Steffen, "Méthodes holographiques de contrôle automatique de pièces mechaniques", first part, Schweizerische Technische Zeitschrift, (1-2), (1978), pp. 27-31.
4. J. Steffen, "Méthodes holographiques de contrôle automatique de pièces mechaniques", second part, Schweizerische Technische Zeitschrift, (3-4), (1978), pp. 73-75.
5. R.S. Sirohi, A Course of Experiments with He-Ne Laser, (Wiley), 1985.
6. M. Born and E. Wolf, Principles of Optics, 6th Ed., (Pergamon Press), 1980.
7. Matlab is available from The MathWorks, Inc., 24 Prime Park Way, Natick, MA 01760-1500. E-mail info@mathworks.com, URL http://www.mathworks.com/.
8. William Press, et.al., Numerical Recipes in C, 2nd Ed. (Cambridge), 1992.
9. The FFT program, originally written in FORTRAN by R.C. Singleton, has been converted to C and revised by John Beale and Mark Olesen. It is in the Netlib archives at http://www.netlib.org/.
10. XFIG, an object-oriented drawing program for the X window system is available at ftp://ftp.x.org/contrib/applications/drawing_tools/efig/.

## FACULTY SPONSORS

Dr. Paul A. DeYoung
Dr. Catherine Mader
Department of Physics
Hope College
Holland, MI 49422-9000

# EFFECTS OF A TRAIN OF SHORT LASER PULSES ON A LORENTZ MODEL ATOM

Rebecca L. Fraser
Department of Physics
Drew University
Madison, NJ 07940
received Nov 22, 1997

**ABSTRACT**

We investigated the interaction of a train of short laser pulses and an isolated Lorentz (classical harmonic oscillator) model atom. Our classical results are derived from the classical Rabi problem. We study the behavior of the atom at a detuning value where the second pulse removes all of the energy from the atoms. We compare our classical results with those obtained by other investigators using the optical Bloch equations. From the Bloch equations, we expect agreement for laser pulses of low intensity. However, we find that the agreement extends to cases where the pulses are large enough to significantly depopulate the lower level.

## INTRODUCTION

In this article, we study the response of an Lorentz model atom to a train of otpical pulses. The electric field of the optical beam creates a dipole moment in the atom. The Lorentz model atom assumes a restoring force proportional to the displacement of the electrom from the proton. This atom acts as if the electron were attached to the proton by a "spring" (the Lorentz model is discussed in many optics books). The optical Bloch equations [1], which model the dynamics of stimulated upward and downward transitions for a set of spins when a magnetic field is swept linearly with time through a resonanace condition, include quantum mechanical effects. We use only the Lorentz model atom in our calculations and, therefore, do not study the optical Bloch Equations directly. We do, however, compare our calculations with the optical Bloch derived results of other investigators.

We consider the case of a train of square optical pulses that can be created by blocking or chopping a cw single-mode laser beam. The laser beam is periodically chopped rather than turned off. An implication of using a chopped cw laser beam is that each pulse is a portion of a continuous sine wave. The portions of the sine wave in the pulse are not identical unless the chopping period is an integer multiple of the optical period. Our case is different from the case of two identical pulses which could be produced, for example, by using a beam splitter and sending one pulse through a delay time. a detailed discussion of the implications ofusing either of these types of pulses can be found elsewhere. [2]

## THE MODEL

The system we will be investigating is a Lorentz model atom in a chopped laser field. The train of square laser pulses has a low duty cycle [3], as illustrated in Figure 1. The duration of time when the laser pulse is 'on' is labeled $t_p$, the time when it is 'off' is labeled $t_d$ and the entire cycle time is labeled $t_r$. We use the word 'off' to describe the time periods when the laser beam is not interacting with the atom even though the beam is chopped rather than the laser turned off.

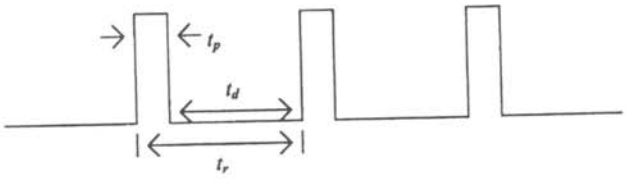


*Figure 1*
*Square optical pulses where $t_p$ represents the pulse time, $t_d$ represents the dead time, $t_r$ represents the total cycle time and $t_r >> t_p$.*

*Rebecca is a sophomore psychology major and physics minor at Drew University. This research was conducted during the summer after her freshman year under an NSF grant at Stevens institute of Technology. She plans to graduate in the year 2000 and then go on to graduate school. Rebecca enjoys running, spending time at the shore and taking day trips with her family and boyfriend in her free time.*

While the pulse is 'on', the equation of motion of the atom is:

$$\ddot{x} + 2\,\beta\,\dot{x} + \omega_o^2 = A\cos(\omega t)\ , \qquad (1)$$

where $\beta$ describes friction, $\omega_o$ is the undamped natural frequency of the oscillator and $A = eE(t)/m$, where $e$ is the charge on the electron, $E(t)$ is the optical field and $m$ is the mass of the electron.

Using the method of the classical Rabi problem [5], we make a shift from the '$x$' notation, which follows the motion of the electron in the atom, to '$u$' and '$v$' notation by implementing a change of variables

$$x(t) = x_o\,\{u(t)\cos(\omega t) - v(t)\sin(\omega t)\}\ , \qquad (2)$$

where $x_o$ is a constant and $\omega$ is the frequency of the laser. The importance of making this change of variables is that the new variables describe the envelope of $x(t)$ and are easier to keep track of since they vary more slowly than $x(t)$. The variable $u$ tracks the part of the dipole moment which is in phase with the optical field, while the variable $v$ tracks the part of the dipole moment which is 90° out of phase with the optical field.

We substitute Equation 2 into Equation 1 and separate the terms multiplying $\sin(\omega t)$ from the terms multiplying $\cos(\omega t)$. [4] Since the sine and cosine are linearly independent functins, the coefficients of each must be identically zero. Collecting terms and solving for $\dot{u}$ and $\dot{v}$ yields:

$$\dot{u} = -\Delta v - \beta u \qquad (3)$$

$$\dot{v} = \Delta u - \beta v - \kappa E\ , \qquad (4)$$

where $\kappa E = A/(2x_o\omega)$ and $\Delta = (\omega_o - \omega)$, the difference between the natural frequency of the atom and the laser frequency. We have dropped terms using the slowly varying envelope approximation:

$$\dot{u} << \omega\, u \quad \dot{v} << \omega\, v$$
$$\ddot{u} << \omega^2\, u \quad \ddot{u} << \omega^2\, u\ . \qquad (5)$$

Since we are considering the case near resonance, where $\Delta$ is much smaller than $\omega$, , we use the approximation:

$$\omega_o + \omega \approx 2\,\omega\ . \qquad (6)$$

We neglect friction during the short periods of time, $t_p$, when the laser is 'on' and include friction for the longer periods of time when the laser is 'off'. Solving Equations 3 and 4 for $u$ and $v$ with $\beta = 0$ (when the pulse is 'on') gives:

$$\begin{bmatrix} u(\tau) \\ v(\tau) \\ 1 \end{bmatrix} = \begin{bmatrix} \cos(\Delta\tau) & -\sin(\Delta\tau) & -\kappa E\left(\frac{1}{\Delta} - \frac{\cos(\Delta\tau)}{\Delta}\right) \\ \sin(\Delta\tau) & \cos(\Delta\tau) & \kappa E\left(\frac{\sin(\Delta\tau)}{\Delta}\right) \\ 0 & 0 & 1 \end{bmatrix} \begin{bmatrix} u_o \\ v_o \\ 1 \end{bmatrix} \qquad (7)$$

where $\kappa E$ is a constant because we are considering square pulses, and $\tau$ is the time elapsed since the start of the current pulse. Equation 7 gives the time evolution of $u$ and $v$ without friction. To find the values of $u$ and $v$ at the end of the pulse, $\tau$ is replaced with $t_p$.

For the longer period of time when the laser is 'off', we include friction. $\kappa E = 0$, since the electric field from the laser is no longer present. Solving Equation 3 and 4 for $u$ and $v$ in this case yields:

$$\begin{bmatrix} u(\tau) \\ v(\tau) \\ 1 \end{bmatrix} = \begin{bmatrix} e^{-\beta\tau}\cos(\Delta\tau) & e^{-\beta\tau}\sin(\Delta\tau) & 0 \\ e^{-\beta\tau}\sin(\Delta\tau) & e^{-\beta\tau}\cos(\Delta\tau) & 0 \\ 0 & 0 & 1 \end{bmatrix} \begin{bmatrix} u_p \\ v_p \\ 1 \end{bmatrix}\ , \qquad (8)$$

where $u_p$ and $v_p$ are the values of $u$ and $v$ at the beginning of the interval considered, the values of $u$ and $v$ at the end of the previous pulse. To find the values of $u$ and $v$ at the end of the 'off' time, the beginning of the next pulse, we replace $\tau$ with $t_d$ in Equation 8.

We now have the solutions for both the time periods: when the laser beam is 'on' and when the laser beam if 'off'. With these solutions we can make plots of polarization (either $v$ or $u$) vs time; or polarization vs detuning $\Delta$ at any fixed time; or the oscillator energy vs time or detuning.

In our case, the oscillator energy is proportional to the square of the amplitude of $x(t)$, as with any simple harmonic oscillator. The square of the amplitude of $x(t)$ is equal to $(u^2 + v^2)$. Figure 2 shows the oscillator energy (in arbitrary units) versus detuning at the end of the second pulse. The bumps seen in Figure 2 are known as Ramsey fringes [7]. The solid line shows our results, while the dashed line shows Thomas' quantum mechanical results.

Figure 2 is interesting as it illustrates an occurrence of what we nicknamed 'killer' pulses. These 'killer' second pulses occur at the detuning values where the energy

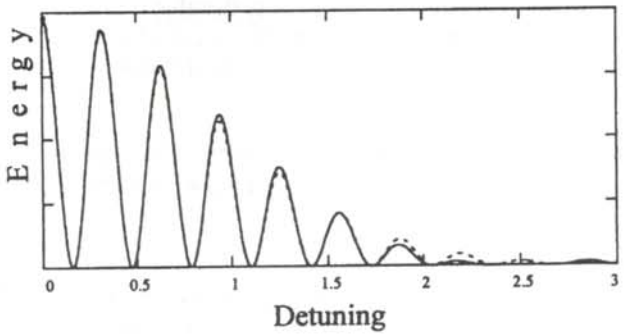


*Figure 2*
*Oscillator energy at the end of the second pulse versus detuning with $\beta = 0$, $t_p = 2.54$ ns and $t_r = 20$ ns for an oscillator starting at rest. The solid line shows our results and the dashed line shows results for a Gaussian pulse train as determined by Thomas. [7]*

reaches zero. At those particular detuning values, when the second pulse hits the atom, it removes all of the energy from the atom instead of adding energy to the atom. This happens because when the laser is 'on', the atom oscillates at the frequency of the applied field. Once the laser is 'off', the atom begins to oscillate at its natural frequency, drifting out of phase with the laser at a rate given by the detuning. When the laser turns back 'on' at those particular 'killer' detuning values, the phase of the oscillating atom has drifted from the laser in such a way that the two have an unfavorable phase relation. [6] Consequently, the second pulse removes all of the energy from the oscillating atom for those particular detuning values, where $\Delta t_r$ is approximately equal to an odd integer multiplied by $\pi$.

Figure 2 shows excellent agreement with a model that uses a coherent train of Gaussian shaped laser pulses. [7] The dotted line is for low intensity pulses. In Figure 2, $\beta = 0$, $t_p = 2.54$ ns and $t_r = 20$ ns. The values were chosen to match those used for the coherent train of Gaussian shaped laser pulses. The oscillator starts at time 0 with no energy; the values of $u$ and $v$ start at 0.

**Comparison of optical Bloch results with Lorentz model results**

The optical Bloch equations account for quantum mechanical effects and allow consideration of high intensity laser pulse trains [2]:

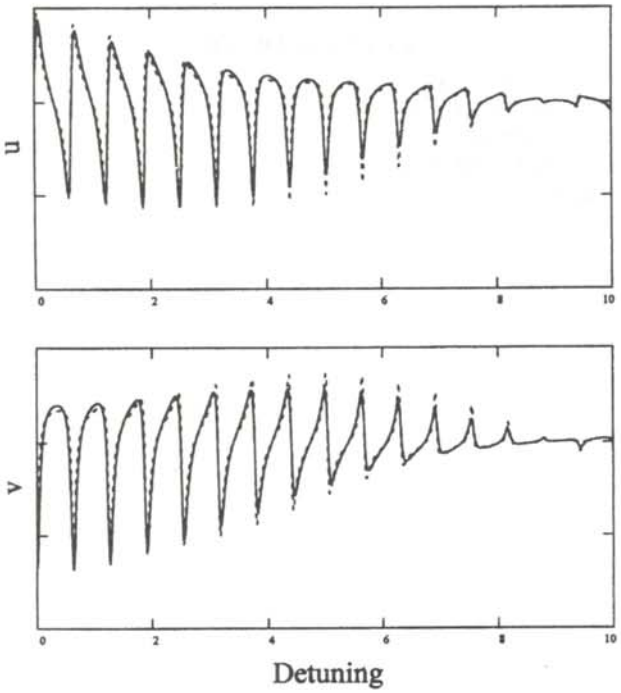


*Figure 3*
*Steady state u and v versus detuning for pulse area of $\pi/8$, $\beta = (16ns)^{-1}$, $t_p = 0.7$ ns and $t_r = 10$ ns. The solid line shows our results and the dashed line shows Temkin's optical Bloch results.*

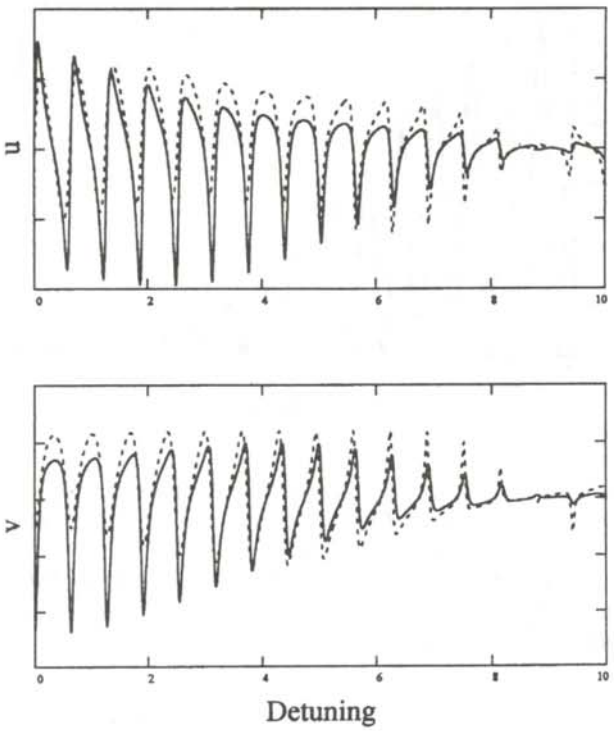


*Figure 4*
*Steady state u and v versus detuning for pulse area of $\pi/2$, $\beta = (16ns)^{-1}$, $t_p = 0.7$ ns and $t_r = 10$ ns. The solid line shows our results and the dashed line shows Temkin's optical Bloch results.*

$$\dot{u} = -\Delta v - \beta u \tag{9}$$

$$\dot{v} = \Delta u - \beta v - \kappa E w \tag{10}$$

$$\dot{w} = -\kappa E w - \gamma(w + 1)\,, \tag{11}$$

where $w$ is a parameter that determines the population inversion. When $w = -1$, the atom is in the ground state, when $w = +1$, the atom is in the upper state. $\gamma$ determines the population decay rate. For example, in the absence of an optical field ($\kappa E = 0$), Equation 11 immediately shows than an atom in the upper state ($w = +1$) would decay back to the ground state according to $w = 2e^{-\gamma t} - 1$. We expect our results to agree with the optical Bloch results when the energy is low and the pulse area is small. At these conditions, $w \approx -1$, which causes Equation 9 and 10 to become Equations 3 and 4 which we used in our classical calculations.

To compare our results with Temkin's Bloch results [3], we plot the steady-state values of polarization versus detuning. We plot $u$ and $v$ at the instant that the pulse turns back 'on' for the $n^{th}$ time versus detuning, where $n$ is any number large enough so that there are no more transients. We choose $t_p = 0.7$ ns, $t_r = 10$ ns and $\beta = (16ns)^{-1}$.

Figure 3, with the pulse area in the Bloch results set equal

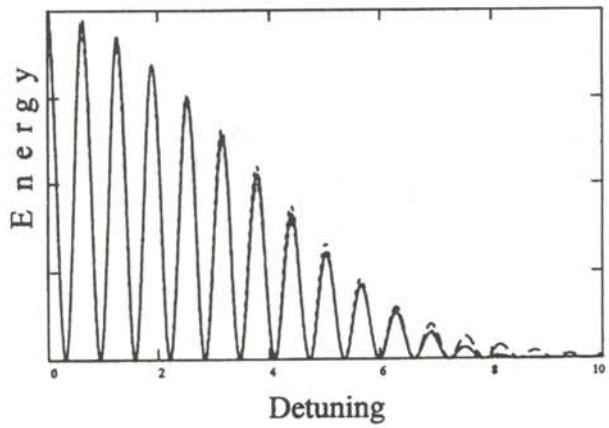


*Figure 5*
*Oscillator energy at the end of the second pulse versus detuning for an area of $\pi/4$, $b = 0$, $t_p = 0.7$ ns and $t_r = 10$ ns for an oscillator starting at rest. The solid line is our results, the short dashed line Temkin's optical Bloch results and the longer dashed line the results using Thomas' Gaussian pulse train.*

to $\pi/8$, shows close agreement between our results (the solid line) and the Bloch results (dotted line). Figure 4, with pulse area of the pulse in the Bloch results set equal to $\pi/2$, illustrates significant disagreement, but still closer agreement that we initially would have expected for a pulse are of that size. We saw similar results for the polarization values at the end of the second pulse versus detuning graphs.

Figure 5 shows the oscillator energy at the end of the second pulse versus detuning with the same values of $t_p$ and $t_r$ used in Figures 3 and 4 and $\beta$=0. The oscillator starts with zero energy, so $u$ and $v$ start with values equal to zero. We include in Figure 5 our results (solid line), Temkin's optical Bloch results (short dashed lines) and Thomas' Gaussian pulse train (long dashed lines). We had to generate the Bloch results for the oscillator energy at the end of the second pulse from equations found in reference 2.

Figure 5 shows significant agreement between all three results. This is surprising since the pulse area of $\pi/4$ is quite large. The results agree less closely as we considered cases of larger pulse areas.

Our results illustrate that we can put our classical intuition to use in cases where it seems that only quantum intuition can be used. Our classical results agree with those predicted by the Bloch equations. We found that this agreement continued for pulse areas large enough to significantly depopulate the lower state, where it would seem that the classical results should fail.

## ACKNOWLEDGMENTS

The work presented in this paper was done during the summer of 1997 at Stevens Institute of Technology in Hoboken, NJ. It was supported by the Research Experience for Undergraduates program of the National Science Foundation at Stevens Institute of Technology under NSF Grant #DMI-9313320.

The author would like to thank Dr. J. Supplee for the time, information and advice he gave and thanks Professor E.A. Whittaker for the opportunity to do this work. The author would also like to thank Mr. J.T. Woodward and Mr. W.J. Fraser for inspiring her to explore physics in college.

## REFERENCES

1. F. Bloch, Phys. Rev., 70, (1946), p. 460.
2. N.V. Vitanov and P.L. Knight, "Coherent Excitation of a Two-State System by a Train of Short Pulses.", Phys. Rev. A, 52, 3, (1995), pp. 2245-2261.
3. R.J. Temkin, "Excitation of an Atom by a Train of Short Pulses", J. Opt. Soc. Am. B, 10,5, (1993), pp. 830-839.
4. P.W. Milonni and J.H. Eberly, Lasers, (Wiley and Sons), 1988, pp. 27-33.
5. L. Allen and J.H. Eberly, Optical Resonance and Two-Level Atoms, (Dover), 1987, pp. 5-7.
6. L.C. Bradley, "Pulse-train Excitation of Sodium for Use as a Synthetic Beacon", J. Opt. Soc. Am. B, 9, 10, (1992), pp. 1931-1944.
7. G.F. Thomas, "Pulse Train Single-Photon Induced Optical Ramsey Fringes", Phys. Rev. A, 35, 12, (1987), pp. 5060-5063.

## FACULTY SPONSOR

Dr. James M. Supplee
Department of Physics
Drew University
Madison, NJ 07940-4037
jsupplee@drew.edu

## PREPARING A MANUSCRIPT FOR PUBLICATION

Rexford E. Adelberger, Editor

Perhaps the most important thing for you to keep in mind when you write a manuscript which you intend to submit for publication to the Journal of Undergraduate Research in Physics is that the audience that will be reading the paper is junior or senior physics majors. They are knowledgeable about physics, but unlike you, they have not spent as much time trying to understand the specific work which is being reported in your paper. They also can read English well, and expect the paper to be written by a colleague, not a robot or an 'all-knowing' computer. There is a big difference between the comments you write in the margin of your lab notebook or what you might write in a technical brief and what you should present in a paper for publication in a scientific journal.

There is a significant difference between a Journal article and keeping a journal. Your laboratory data book should be the journal of what you did. It contains all the data, what you did (even if it was an attempt that turned out to be wrong), as well as comments as to what you were thinking at that time. The Journal article is an discussion of how you would do the research without excursions along blind alleys and hours spent collecting data that were not consistent. The reader should not necessarily be able to completely reproduce the work from the Journal article, but the reader should be able to understand the physics and techniques of what was done.

How a person uses Journal articles to find out about new ideas in physics is often done in the following way. A computerized search, using key words in abstracts, is performed to find what work others have done in the area of interest. If the abstract seems to be about the question of interest, the body of the paper is tracked down and read. If the reader then wants to find out the finer details of how to reproduce the experiment or the derivation of some equation, the author of the paper is contacted for a personal in-depth conversation about the more subtle details.

The general style of writing that should be followed when preparing a manuscript for publication in the Journal is different from what you would submit to your English literature professor as a critique of some other work. The narrative of the paper is intended to do three things: 1) present the background necessary for the reader to appreciate and understand the physics being reported in the paper; 2) discuss the details of what you did and the implications of your work; 3) lead the reader through the work in such a way that they must come to the same concluding points that you did. When finished with your paper, the reader should not have to go back and try to decide for themselves what you did. Your narrative should lead them through your work in an unambiguous manner, telling them what to see and understand in what you did. The interpretation of the data or calculations should be done by the writer, not the reader. The interpretation of your results is the most important part of the paper.

You should take care to make sure that the material is presented in a concise logical way. You should make sure that your sentences do not have too many dependent clauses. Overly complicated sentences make the logic of an argument difficult to follow. You should choose a paragraph structure that focuses the attention of the reader on the development of the ideas.

A format which often achieves these aims is suggested below:

**ABSTRACT** : An abstract is a self contained paragraph that concisely explains what you did and presents any interesting results you found. The abstract is often published separately from the body of the paper, so you cannot assume that the reader of the abstract also has a copy of the rest of the paper. You cannot refer to figures or data that are presented in the body of the paper. Abstracts are used in computerized literature searches, so all key words that describe the paper should be included in the abstract.

**INTRODUCTION**: This is the section that sets the background for the important part of the paper. It is not just an abbreviated review of what you are going to discuss in detail later. This section of the narrative should present the necessary theoretical and experimental background such that a knowledgeable colleague, who might not be expert in the field, will be able to understand the data presentation and discussion. If you are going to use a particular theoretical model to extract some formation from your data, this model should be discussed in the introduction.

Where appropriate, factual information should be referenced using end-notes. When presenting background information, you can guide the reader to a detailed description of a particular item with the statement such as: *"A more detailed discussion of laminar flow can be found elsewhere [1]"*. If you know where there is a good discussion of some item, you don't have to repeat it, just guide the reader to the piece.

How one proceeds from this point depends upon whether the paper is about a theoretical study or is a report on an experiment. I will first suggest a format for papers about experimental investigations and then one that describes a theoretical derivation.

### *Experimental Investigations*

**THE EXPERIMENT**: This section guides the reader through the techniques and apparatus used to generate the data. Schematic diagrams of equipment and circuits are often easier to understand than prose descriptions. A statement such as *"A diagram of the circuit used to measure the stopping potential is shown in Figure 6"* is better than a long elegant set of words. It is not necessary to describe in words what is shown in a diagram unless you feel that there is a very special part which should be pointed out to the reader. If special experimental techniques were developed as part of this work, they should be discussed here. You should separate the discussion of the equipment used to measure something from your results. This section should not include data presentations or discussions of error analysis.

**DATA PRESENTATION AND INTERPRETATION OF RESULTS**: This is the most important section of the paper. The data *(a plural noun)* are the truths of your work. This section should lead the reader through the data and how errors were measured or assigned. The numerical data values are presented in tables and figures, each with its own number and caption, e.g.. *"The results of the conductivity measurements are shown in Table 3"*. It is difficult to follow narratives where the numerical results are included as part of the narrative. Raw, unanalyzed data should not be presented in the paper. All figures and tables should be referred to by their number. Any figure or table that is not discussed in the narrative should be eliminated. Items which are not discussed have no place in a paper.

### *A Theoretical Study*

**THE MODEL**: This part should consist of a theoretical development of the constructs used to model the physical system

under investigation. Formulae should be on separate lines and numbered consecutively. The letters or symbols used in the equations should be identified in the narrative, e.g.. *The potential can be approximated as:*

$$W \approx Z - \sigma(\rho) \ , \qquad (1)$$

*where Z is the number of protons and σ is the screening constant that is dependent on the charge density, ρ, of the inner electrons of the K and L shells.* If you wish to use this formula at a later time in the narrative, you refer to it by its number, e.g.. "*The straight line fit shown in Figure 3 means that we can use Equation 1 to extract a value of...*"

**CALCULATIONS**: This section presents a summary and discussion of the numerical results calculated from the model. The results should be presented in tables or graphs, each with a caption. A table or graph which is not discussed in the narrative should be eliminated. Data that are not interpreted by the writer have no place in a paper. One should reference numerical results that are used in the calculations and come from previous work done by others .

**The following sections pertain to both types of papers.**

**CONCLUSIONS**: It is indeed rare that one can come to clear and meaningful conclusions in one paper. I do not know of many papers where this section should be included.

**REFERENCES**: All references, numbered in order from beginning to end of the paper, are collected together at the end of the paper. You should be aware of the following format:

*If the reference is a text-*

1. A.J. Smith and Q.C.S. Smythe, Electromagnetic Theory, Addison Wesley, New York, (1962), p. 168.

*If the reference is a journal-*

2. J. Boswain, Journal of Results, 92, (1968), pp. 122-127.

*If the reference is unpublished-*

3) R.J. Ralson, private communication.

**ACKNOWLEDGMENTS**: This short section should acknowledge the help received (that is not referenced in the previous section) from others. This is where you would give credit to a lab partner or someone in the machine shop who helped you build a piece of equipment.

## OTHER ADVICE

**TABLES AND FIGURES** are placed by the layout editors at the corners of the page to make the format attractive and easy to read. Often a figure is not on the same page as the discussion of the figure. Each table or figure should be numbered and have a caption which explains the figure. Readers scan papers by looking at the figures and data tables before they read the narrative of the work. Take care to put enough information in the caption of a figure or table so that the reader can get some feeling for the meaning of the data presentation. All lines shown on graphs should be identified, e.g.. *"The dashed line is drawn to guide the eye"* or *"The solid line is a fit to the data using the Ising model"*

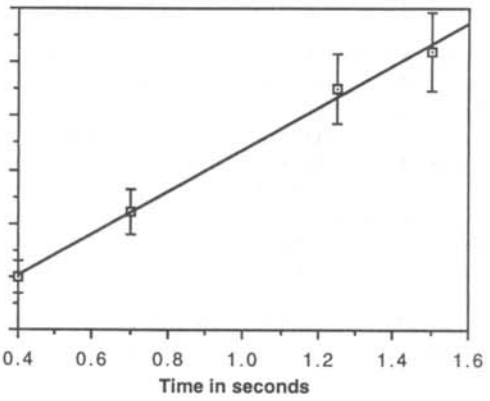


*Figure 1*

*A graph of the measured thrust of a D-2 model rocket engine as a function of time. The line drawn is the least squares fit straight line to the data.*

| *State* | *Experimental eV* | *Theoretical eV* |
|---|---|---|
| *3S* | *5.15±01* | *5.13* |
| *4S* | *1.89±02* | *1.93* |
| *3P* | *2.96±02* | *3.02* |

*Table 1*

*Energy states found in the numerical search. The accepted values for these states are also listed.*

An example of a graph of a set of data is shown in Figure 1. The graph is sized by the range of data points. The bottom left point does not have to be the point (0,0). Error bars are shown with the data points. A graph with all the data points clustered in one small corner and lots of white space does not help the reader get a feeling of the dependence of your data. Be careful that the figures you present are not too busy; too much information on a figure makes it difficult to pick out the important parts.

**NUMBERS AND UNITS** Any experimentally measured data presented in tables (such as shown in Table 1), should include an uncertainty. You should use scientific notation when presenting numbers, $(7.34 \pm .03) \times 10^7$ eV. Take care that you have the correct number of significant digits in your results; just because the computer prints out 6 digits does not mean that they are significant. You should use the MKS system of units.

**STYLE** It is often helpful to make a flow chart of your paper before you write it. In this way, you can be sure that the logical development of your presentation does not resemble two octopuses fighting, but that it is linear.

One generally writes the report in the past tense. You already did the experiment. You also should use the third person neuter case. Even though you might have done the work by yourself, you use "we". e.g.. *"We calculated the transition probability for..."* It is often confusing when you begin sentences with conjunctions. Make sure that each sentence is a clear positive statement rather than an apology.

There are a few words or phrases you should be careful about using. ***Fact*** - this is a legal word. I am not sure what it means in physics. ***Proof or prove*** - These words are meaningful in mathematics, but you can't prove something in physics, especially experimental physics. ***The purpose of this experiment is...*** Often it is necessary to do the experiment to complete the requirements for your degree. You do not need to discuss the purposes of the experiment. ***One can easily show that...*** - Don't try to intimidate the reader. What if the reader finds it difficult to show? Remember that the reader of your paper is a senior in college! ***It is obvious that... or One clearly can see....*** - Such statements only intimidate the reader that does not find your work trivial. What is obvious to someone who has spent a lot of time thinking about it may not be obvious to the reader of your paper.

# The Journal of Undergraduate Research in Physics

***The Journal of Undergraduate Research in Physics*** is the journal of Sigma Pi Sigma and the Society of Physics Students. It is published by the Physics Department of Guilford College, Greensboro NC 27410. Inquiries about the journal should be sent to the editorial office.

**The Journal of Undergraduate Research in Physics ISSN 0731-3764**

***Editorial Office -***

The Journal of Undergraduate Research in Physics
Physics Department
Guilford College
Greensboro, NC 27410
336-316-2279 (voice)
336-316-2951 (FAX)

***Editor -***

Dr. Rexford E. Adelberger
Professor of Physics
Physics Department
Guilford College
Greensboro, NC 27410
ADELBERGERRE@RASCAL.GUILFORD.EDU

**The Society of Physics Students**

*National Office -*

Dr. Dwight Neuenschwander, Director
Ms. Sonja Lopez, SPS Supervisor
Society of Physics Students
American Institute of Physics
1 Physics Ellipse
College Park, MD 20740
301-209-3007

***President of the Society -***

Dr. Robert Fenstermacher
Department of Physics
Drew University

***President of Sigma Pi Sigma -***

Dr. Jean Krisch
Department of Physics
University of Michigan, Ann Arbor